Depth-Resolved Defect Characterization of Multi-Layer Thin-Film Semiconductor Materials via Positron Annihilation Spectroscopy

Jack Driscoll

December 2023

Abstract

This dissertation details the novel application of UTA's advanced variable-energy positron beam to the study of multi-layer thin-film semiconductor materials. By varying the energy of the incident positrons, thereby modifying their implantation depth, we demonstrate that the beam has the capability to perform layer-specific measurements of defect concentrations of semiconductor heterostructures. This thesis also details a number of repairs and upgrades to the beamline which were required in order to facilitate these measurements, primarily the repair of a cryogenic positron moderator and the design and construction of a monostable multivibrator circuit used to upgrade our coincident gamma ray measurement system.

Contents

Chapter 1

Theory

1.1 The Positron

The positron is the antiparticle to the electron. As such, it has the same spin and mass as the electron, but a charge of +e instead of the -e charge held by the electron. It was postulated to exist by Paul Dirac in his 1928 paper, which proposed that electrons could possess both positive and negative charges.[1] In this paper, Dirac introduced the Dirac equation, which is a relativistic wave equation governing all massive spin-$\frac{1}{2}$ particles.

$$(i\hbar\gamma^{\mu}\partial_{\mu} - mc)\psi(x) = 0 \tag{1.1}$$

The positron was officially discovered on August 2nd 1932 by Carl David Anderson by allowing cosmic rays to pass through a Wilson cloud chamber under influence of a magnetic field.[2] By observing a particle which had a trajectory curvature corresponding to a mass-to-charge ratio equal to that of an electron, but with a curvature in the opposite direction, Anderson was able to demonstrate the existence of the positron, which had the further implication of proving that antimatter in general could exist. This experiment would win him the 1936 Nobel prize, which he would share with Victor Franz Hess for the discovery of cosmic radiation.

When a positron collides with an electron, the two annihilate with each other. In the annihilation process, an electron positron pair is destroyed to create two or more photons. Energy and momentum are conserved in this process, and are distributed among the resultant photons. The creation of a single photon is forbidden by conservation of energy and momentum. The rest mass energy of the positron and electron are 511keV each, and (in the low energy case) the most likely result of the annihilation process is two photons, meaning that each of these photons will, on average, have an energy of 511keV.[3, 4, 5]

The small differences in the energies of the resultant photons is the basis for positron annihilation spectroscopy, or PAS. This technique, which is the main focus of this thesis, leverages the fact that the photons which result from the annihilation process will be non-collinear, and will have differing energies. The distribution of these energies can be attributed to the angular momentum of the electron which is involved in the annihilation process, meaning the distribution of these photon energies can be used to draw conclusions about the electronic environment of the sample under analysis. The dependence of the resultant photon energy distribution on the momentum of the positron-electron pair lead to the earliest PAS technique, known as angular correlation of annihilation radiation (ACAR), which focuses on the non-collinearity of the resultant photons.[6, 7]

Another important behavior of positrons is their ability to form positronium. Positronium is the bound state of the positron and electron, with a ground state binding energy of 6.8eV, which forms prior to annihilation of the two particles, and has two distinct states: para-positronium (p-Ps) and ortho-positronium (o-Ps). Para-positronium is a singlet state in which the electron and positron possess anti-parallel spins. It has a mean lifetime of 0.12ns and, as mentioned previously, preferentially annihilates to form 2 photons whose energies sum to 1.022MeV.[8] While it's possible for para-positronium to emit higher numbers of photons in multiples of two, the probability of higher-photon events decreases rapidly as the number of resultant photons increase (a 4-photon event has a probability of $\sim 10^{-6}$). Ortho-positronium is a triplet state in which the electron and positron have parallel spins.

This state has an energy which is 0.0001eV higher than the singlet state, primarily emits 3 gamma rays instead of 2, and has a lifetime of ∼142ns.[8] In molecular materials, this lifetime depends strongly on the topology of the material under study. Large open volumes (such as those found in zeolites) will cause a drastic reduction in the lifetime of o-Ps as the positron picks up an electron with antiparallel spin from the surrounding environment, allowing the positron to annihilate more rapidly than it otherwise would. This behavior led to a technique known as positron annihilation lifetime spectroscopy (PALS), which is used primarily to study the internal topology of various materials.

With the advent of high-purity germanium radiation detectors, a new technique was able to be developed which, in a method similar to ACAR, leveraged the Doppler shift in the gamma rays due to the momenta of the electron and positron involved in the annihilation process. This technique allows for the study of electron momentum distributions within materials, which can be used to determine a number of properties of the material under analysis, most notably defect concentrations. [9] The spectral peak produced by Doppler Broadening Spectroscopy (DBS) is broken down into two primary regions: the peak center and the "wings".

The center of this peak corresponds to what's known as the S-Parameter, which is defined as the ratio of the integral of the central region of the peak to the integral of the entire peak. This S-Parameter comes mainly from valence band electron annihilation events. Due to the lower orbital angular momentum of the electrons in the valence band, the effect of Doppler broadening will be less significant, and the gamma rays emitted by annihilation events which involve these electrons will be closer to the 511keV peak. In contrast, the W-Parameter is defined as the ratio of the integral of the "wing" regions to the integral of the entire peak, and corresponds to core electron annihilation events and positronium formatio. These regions can be seen in figure 1.1 Due to the higher momenta of core electrons, the Doppler shift is more significant, and these gamma ray energies will have a higher standard deviation than those of the valence electrons.[11]

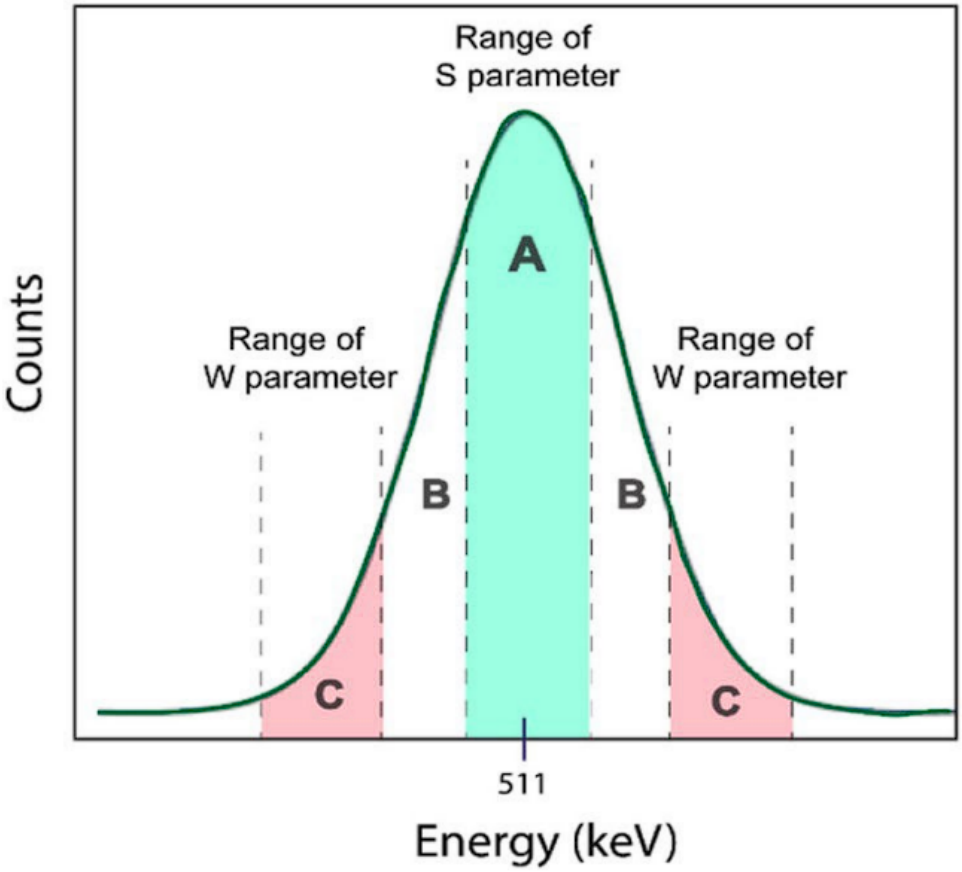

Figure 1.1: S and W parameter regions of a 511keV peak [10]

Another technique which is closely related to PAS is positron-annihilation-induced Auger electron spectroscopy (PAES). When the positron annihilates with an electron in a material, it leaves behind a vacancy in the electron structure of an atom. Subsequently, an electron from a higher-energy state in the atomic structure will fall into this vacancy in order to occupy a lower-energy state. This energy level transition results in a radiative process, whereby the potential energy possessed by the electron in the high-energy state is transferred to another electron within the atom. If this energy is sufficient (most often in the case of valence electrons), the electron which receives this energy will become unbound from the nucleus, being emitted as an Auger electron.[12] A graphical representation of his process can be seen in figure 1.2. Because the energy of this Auger electron depends on the electronic structure of the atom, we can draw conclusions about the physical and chemical characteristics of a material by measuring the kinetic energies of Auger electrons emitted from the material.

1.2 Positrons in Materials

As more research has been done using these various PAS techniques, it has become clear that PAS is a valuable non-destructive method for studying a wide range of material properties and characteristics. There are two primary modes of PAS which have proved to be useful: bulk studies and surface-sensitive studies. The operating mode of a positron experiment depends on the energy of the incident positrons on the sample. Higher energy positrons will embed themselves further within the bulk of the material, and lower-energy positrons will find their way back to the surface, preferentially annihilating with the electrons at or near the surface of the material.

When a positron first comes into contact with a sample, it will either backscatter from the surface, or embed itself within the material. In the case that the positron enters the bulk of the material, it transfers its kinetic energy to the lattice via scattering until it nearly approaches thermal energy.[13] This thermalization process takes a short amount of

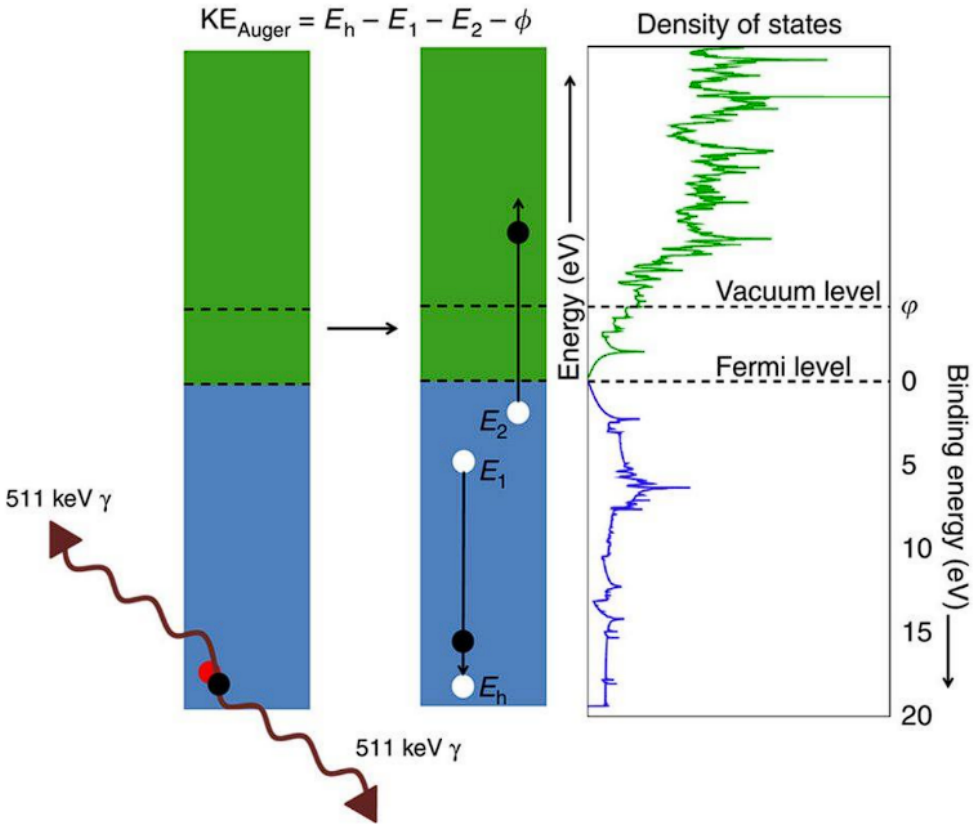

Figure 1.2: VVV Auger emission process: E_h annihilates with the positron, the hole is filled by E_1, and the energy is given to E_2, which is emitted as an Auger electron. The density of states shown on the right is for graphene.[10]

time relative to the total lifetime of the positron within the material (on the order of a few picoseconds), and the probability of a positron annihilating prior to thermalization is minimal.[14, 15] After thermalization, the positron exists as a delocalized charge carrier within the bulk of the material, whose diffusion is governed by the diffusion annihilation equation.

$$\frac{\partial}{\partial t} n(\vec{r}, t) = D_+ \nabla^2 n(\vec{r}, t) - \lambda_B n(\vec{r}, t) \tag{1.2}$$

Where $n(\vec{r}, t)$ is the positron density function, λ_B is the annihilation rate, and the diffusion coefficient D_+ is given by the diffusion coefficient equation, derived from the random walk theory

$$D_+ = \sqrt{\frac{k_B T}{m^*} \tau_r} \tag{1.3}$$

Where k_B is the Boltzmann constant, T is the temperature, m^* is the effective mass of the positron, and τ_r is the scattering relaxation time. Further, we can calculate the positron diffusion length L_{+b} using the following relation

$$L_{+b} = \sqrt{D_+ \tau_B} \tag{1.4}$$

Where τ_B is the lifetime of the positron within a given material.[16, 17] These equations serve as approximations, and rely on a number of classical assumptions, but are nonetheless useful in predicting the behavior of positrons within a material.

As a delocalized positive charge carrier, the amplitude of the positron's wavefunction is at its maximum in the regions farthest away from the nuclei of atoms, due to being repelled from the positively charged ion cores. The wavefunction for the positron in an idealized lattice can be seen in figure 1.3, while figures 1.4, 1.5, and 1.6 show the wavefunction for a positron trapped in a monovacancy, divacancy, and trivacancy, respectively.

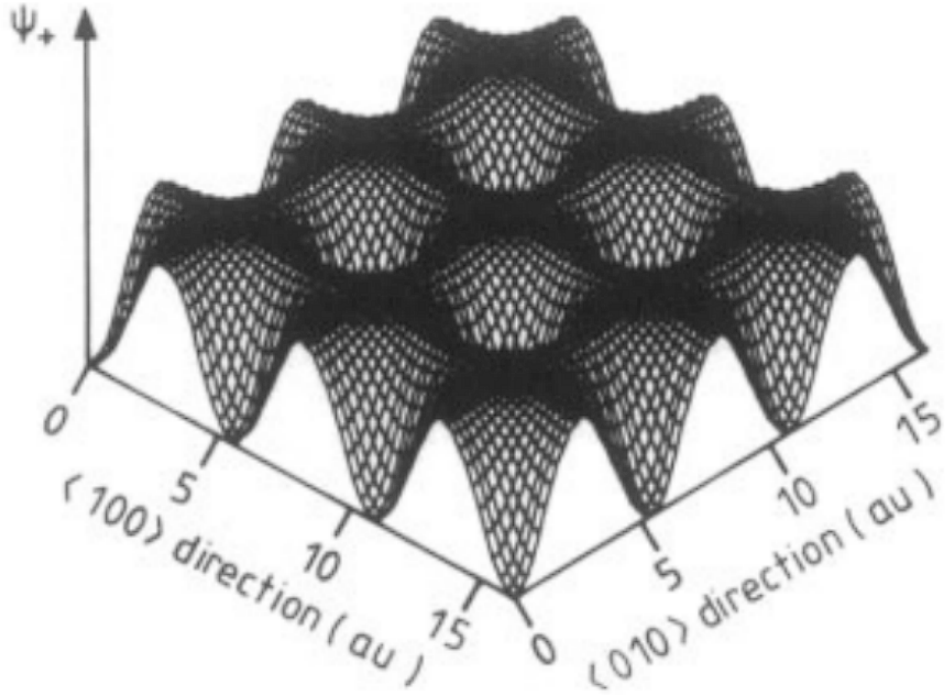

Figure 1.3: Delocalized positron wavefunction in an idealized Fe BCC lattice [18]

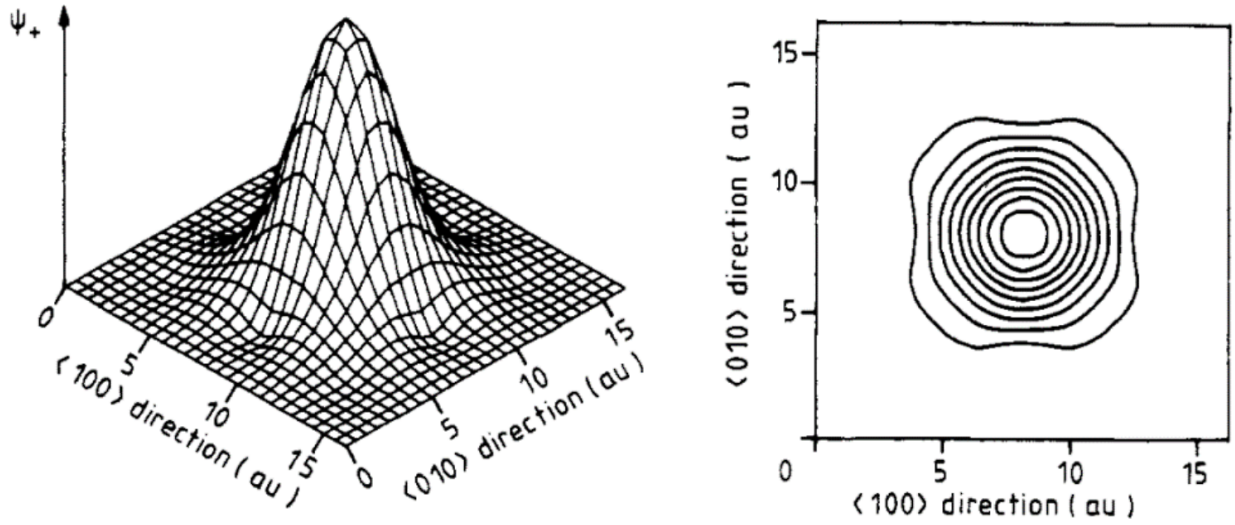

Figure 1.4: Positron monovacancy wavefunction [18]

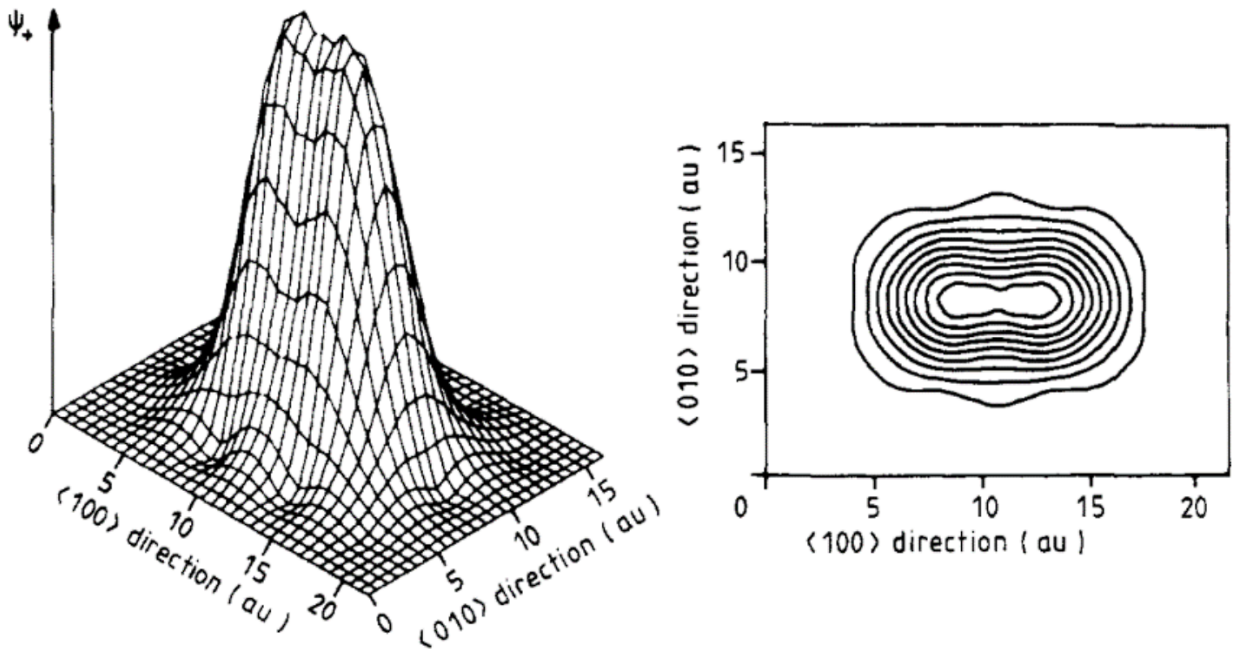

Figure 1.5: Positron divacancy wavefunction [18]

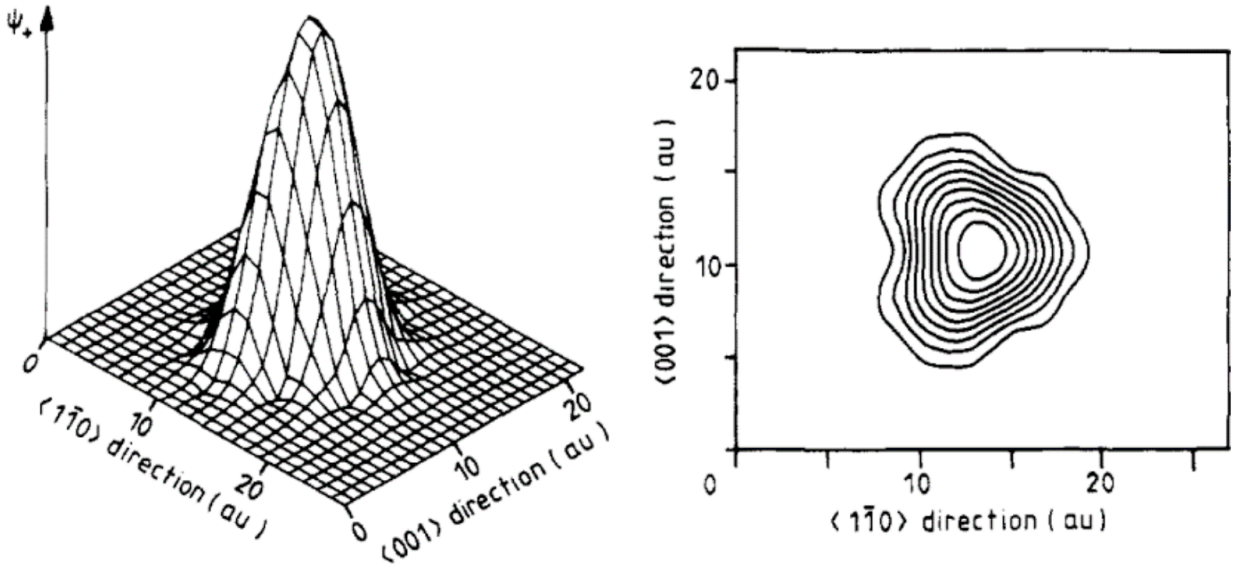

Figure 1.6: Positron trivacancy wavefunction [18]

As the positron continues to diffuse within the bulk of the material, it will preferentially localize within negatively charged defects within the materials. These lattice defects represent a potential minimum from the perspective of the positron due to the absence of positively charged ion cores and presence of negatively charged electrons (especially of the valence level). As such, the positrons will get trapped in the potential wells formed by the lattice defects, where they will annihilate with nearby electrons. As the positron localizes within the vacancy, its wavefunction overlaps more with the outer-shell electrons of the atom, meaning the positrons will annihilate more frequently with conduction electrons. The theoretical contributions from electrons in different shells is shown in figure 1.7; core electrons display a more broad peak than those of the outer shells.

The tendency for the positron to annihilate with the valence electrons means that the contribution to the PAS spectrum from the more energetic core electrons is decreased, as is the electron momentum component of the annihilation process. The doppler shift caused by the electron's momentum can be calculated by leveraging energy and momentum conservation.[19]

$$\frac{E_{\gamma 2} - E_{\gamma 1}}{c} = \vec{p}_{\parallel} \tag{1.5}$$

$$E_{\gamma 1} + E_{\gamma 2} = 2m_0c^2 - E_b \tag{1.6}$$

Where $E_{\gamma 1}$ and $E_{\gamma 2}$ are the energies of the gamma rays, $p_{\parallel}$ is the component of the electron's momentum which is parallel to the gamma rays, m_0 is the rest mass of the electron, and E_b is the binding energy of the electron. With these equations, we can arrive at the expressions for the expected doppler shift (equation 1.7), as well as the energies for each of the gamma rays (equations 1.8 and 1.9).

$$\Delta E_{\gamma} = \frac{E_b \pm c\vec{p}_{\parallel}}{2} \tag{1.7}$$

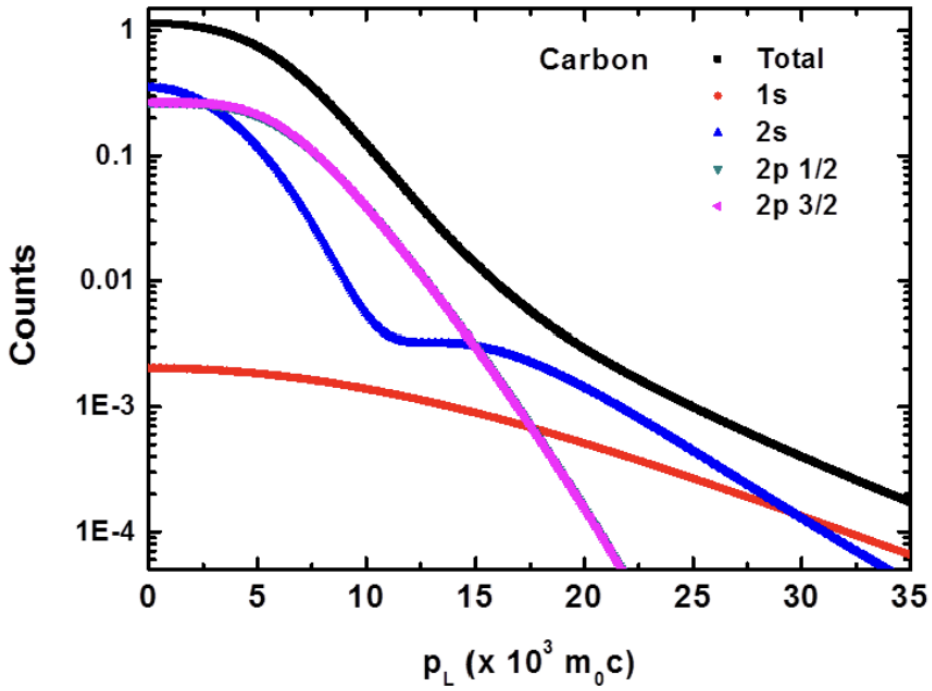

Figure 1.7: Theoretical spectral contributions for different electron shells in carbon. [20]

$$E_{\gamma 1} = m_0 c^2 - \frac{E_b + c\vec{p}_{\|}}{2} \tag{1.8}$$

$$E_{\gamma 2} = m_0 c^2 - \frac{E_b - c\vec{p}_{\|}}{2} \tag{1.9}$$

From this we can see that the annihilation of defect-localized positrons leads to a decrease in the Doppler broadening of the gamma ray spectrum, and increased collinearity of the annihilation gamma rays, which in turn results in a more narrow PAS spectrum, meaning that a defect-free material will produce a more broad gamma peak than a material which contains a high concentration of defects. This is an extremely sensitive technique, and a narrowing of the PAS spectrum can be observed at defect concentrations as low as 10^{-7}.

In many cases, the diffusion of the positron results in a return to the surface, where the positron becomes trapped in a potential well (various positrons interactions are shown in figure 1.8, and their diffusion probabilities are shown in 1.9). This behavior leads to the

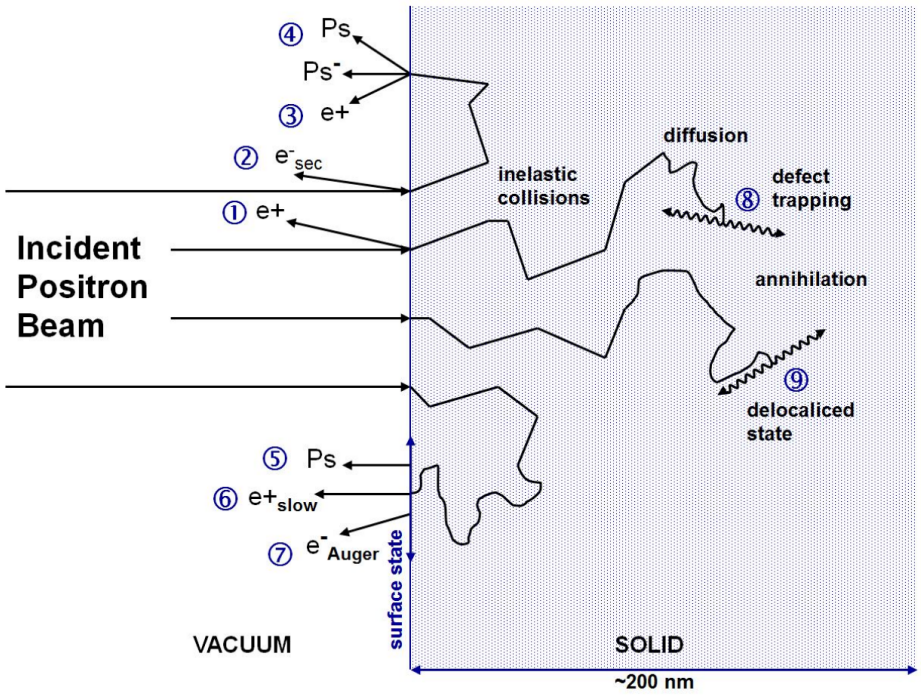

Figure 1.8: This image shows the various ways positrons can interact with a material including delocalized bulk states, bulk annihilation, and the different surface states which arise. [22]

surface-sensitive nature of the PAS technique, and permits us to use PAS to draw conclusions about chemical composition and defect characteristics on the surface.[21, 13] The surface sensitivity of this technique is the result of a two-fold process. The first part in this process is a random walk of the positron which inevitably results in a return to the surface. While reflection from the surface represents a significant percentage of the interactions (22% at $E_+ = 2$keV for high-Z materials such as Au), we concern ourselves only with implanted and diffused positrons, of which our surface-diffused positrons represent about 55%.[22]

As a given positron diffuses back to the surface, it finds its way into a potential well formed by the superposition of the ion cores and conduction electrons (figure 1.10), where it becomes trapped in a localized surface state (figures 1.11 and 1.12). After becoming trapped in this potential well, the significant overlap between the wavefunctions of the positron and surface-state electrons results in a high likelihood that the positron will engage with an electron within the topmost atomic layer of the material, leading to the surface sensitivity

of this technique. This surface sensitivity has been found to be incredibly useful in studying thin-film materials, which are of vital importance to the materials science field, especially with regards to cutting-edge semiconductor devices.

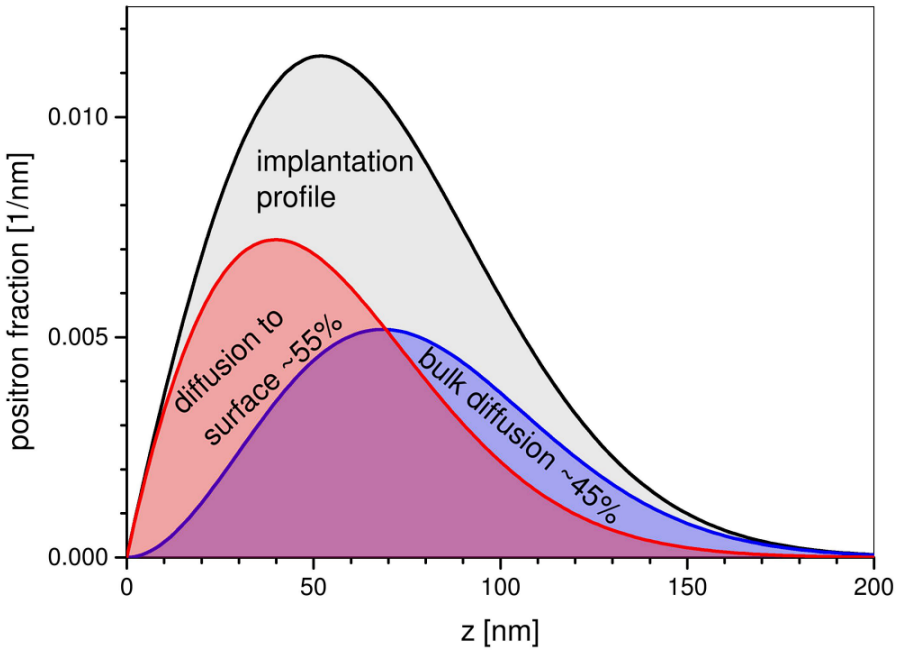

Figure 1.9: Positron implantation profile, which shows the probability of the positron diffusing either to the bulk or the surface with $E_+ = 3\text{keV}$ and $L_{+b} = 100\text{nm}$. [22]

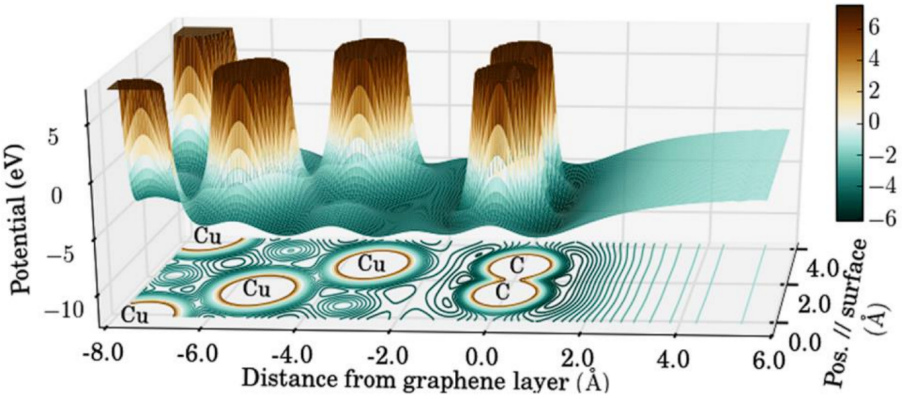

Figure 1.10: Potential of graphene on Cu. [23]

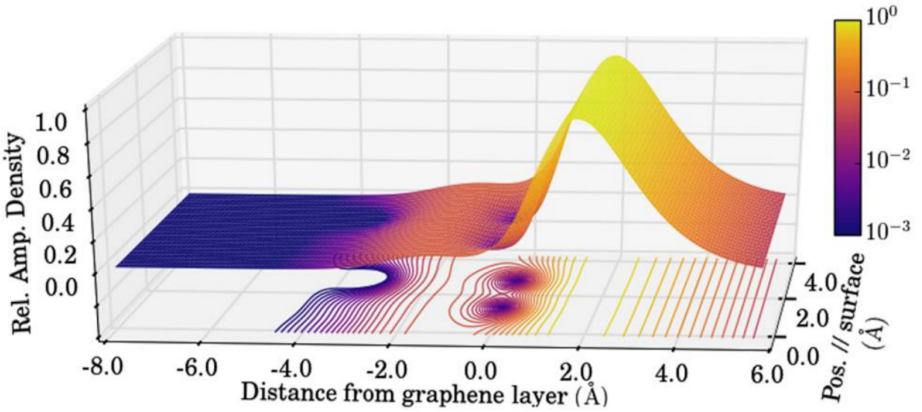

Figure 1.11: Localized positron surface state for graphene on Cu. [23]

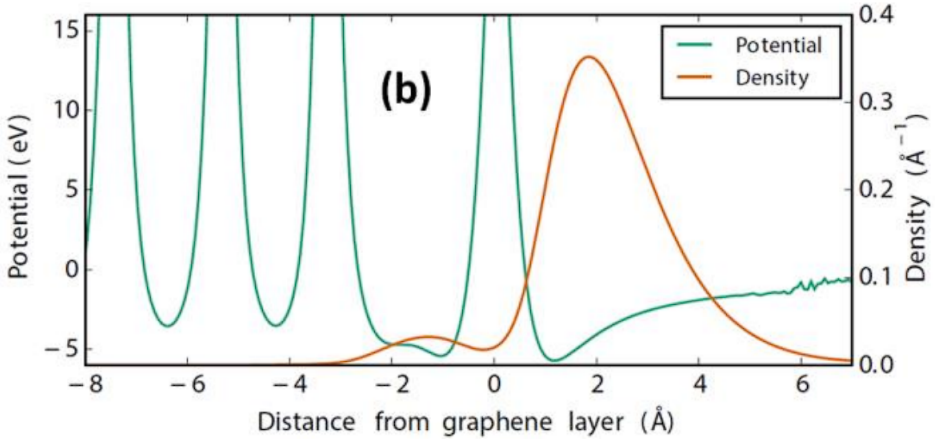

Figure 1.12: 2D overlay of the positron's wavefunction and the surface state potential. Here we see that the positron's probability density is highest within the surface state potential well. [23]

Chapter 2

Positron Beam

2.1 Cryogenic Positron Moderator

The beam starts with the production of positrons from the β^+ decay of a ^{22}Na source. This is a standard source for positron beams, as ^{22}Na has a relatively long half life (2.6 years), and the β^+ decay mode constitutes 90.57% of the radioactive decay process of this isotope (figure 2.1).[24] The source is contained within a small cylindrical titanium capsule 20mm in diameter and 10mm in height, shown in figure 2.2, which sits within a lead housing.

For PAS experiments, it's necessary for us to precisely control the kinetic energies of the incident positrons. To achieve this, we use a rare gas moderator (RGM), which employs solid neon in order to moderate the energies of the incoming positrons. The positron energy spectrum before and after energy moderation is shown in figure 2.3. Tungsten films have been used historically, but the efficiency of tungsten moderators has been found to be on the order of 10^{-4}, where our RGM is able to achieve efficiencies as high as 1%.[26, 27] The drawback to this system is that it is far more complex, and requires a great deal of maintenance to keep in operating condition. It also has a greater deviation in both the energy and direction of the resulting positrons, but the benefit of higher beam intensity makes it worth the trouble. A schematic of the RGM system is shown in figure 2.5.

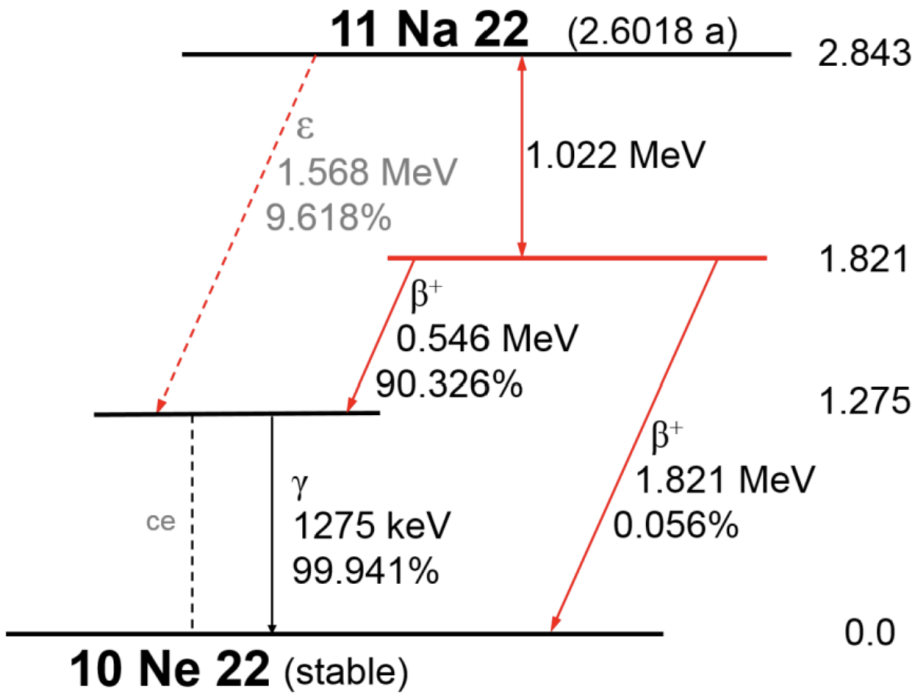

Figure 2.1: Decay mode of ^{22}Na. 90.57% of this process results in the emission of β^+. [24]

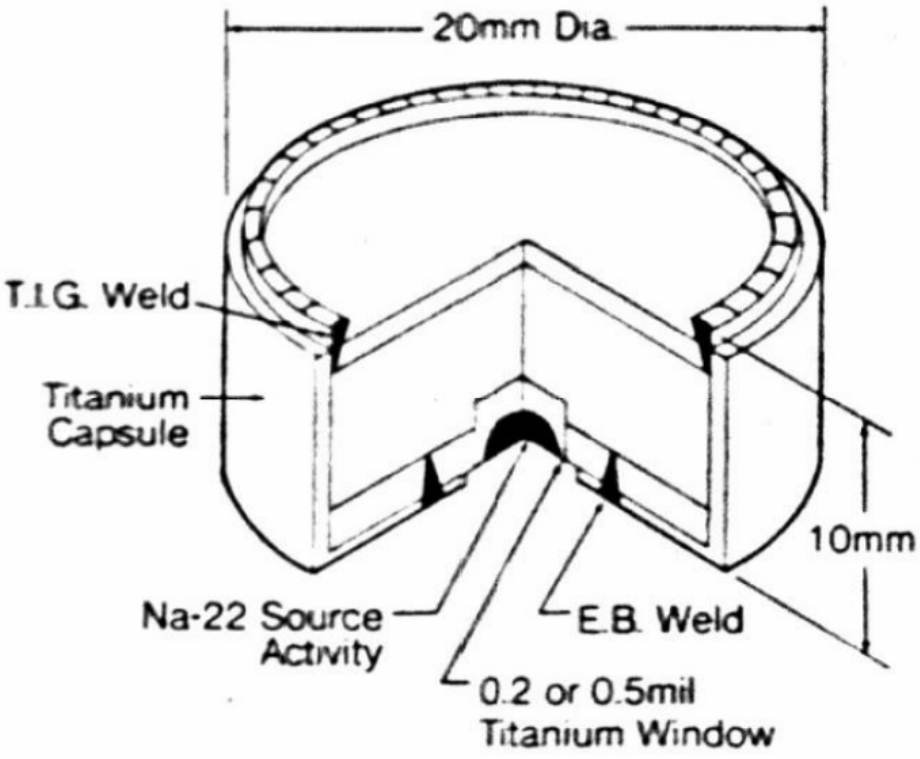

Figure 2.2: The capsule containing the ^{22}Na source. [25]

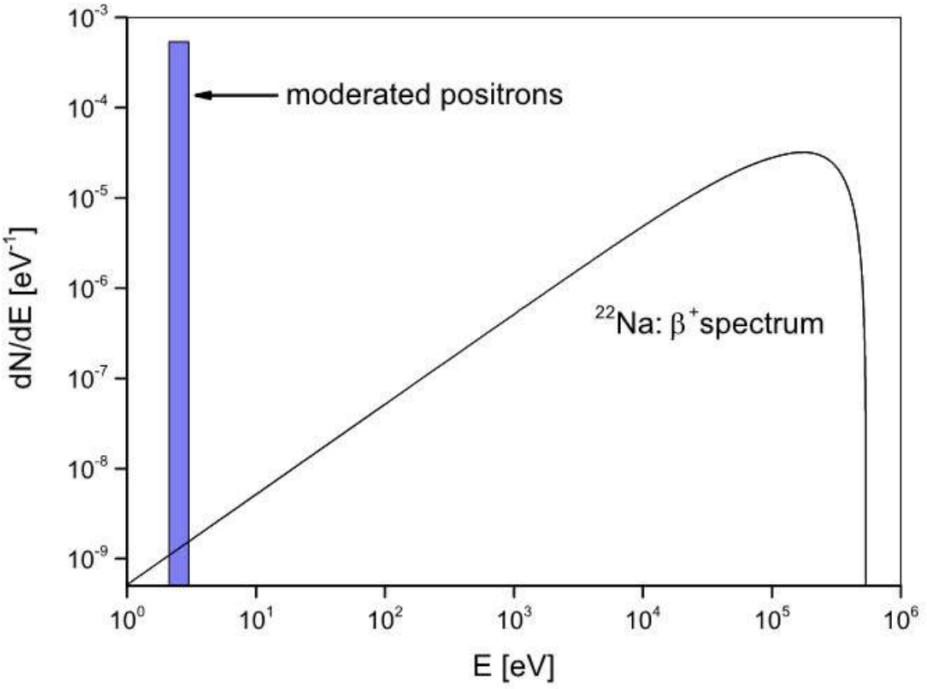

Figure 2.3: Energy spectrum of the positrons before and after moderation. [22]

The positron source sits directly behind the copper cone which acts as the coldhead, onto which the neon gas is frozen and annealed to form the moderator (figures 2.6 and 2.7). The moderator must be grown on a regular basis, as the quality of the solid neon tends to deteriorate over time, thereby reducing the efficiency and intensity of the beam (figure 3.5). This process is mostly automated, and is controlled by a LabView program which was created specifically to interface with this RGM. The growth process happens in 10 stages, which are as follows:

1. Evaporate the old moderator, switch off the ion pump and cold head, open the pumpout valve, and warm the cold head to 23K
2. Wait for 10 minutes, restart the ion pump, and reset the moderator set point to 5K
3. Pump the system for 10 minutes, restart the cold head, and close the roughing valve
4. Wait for the cold head to reach 8.8K
5. Allow the temperature to stabilize for 10 minutes

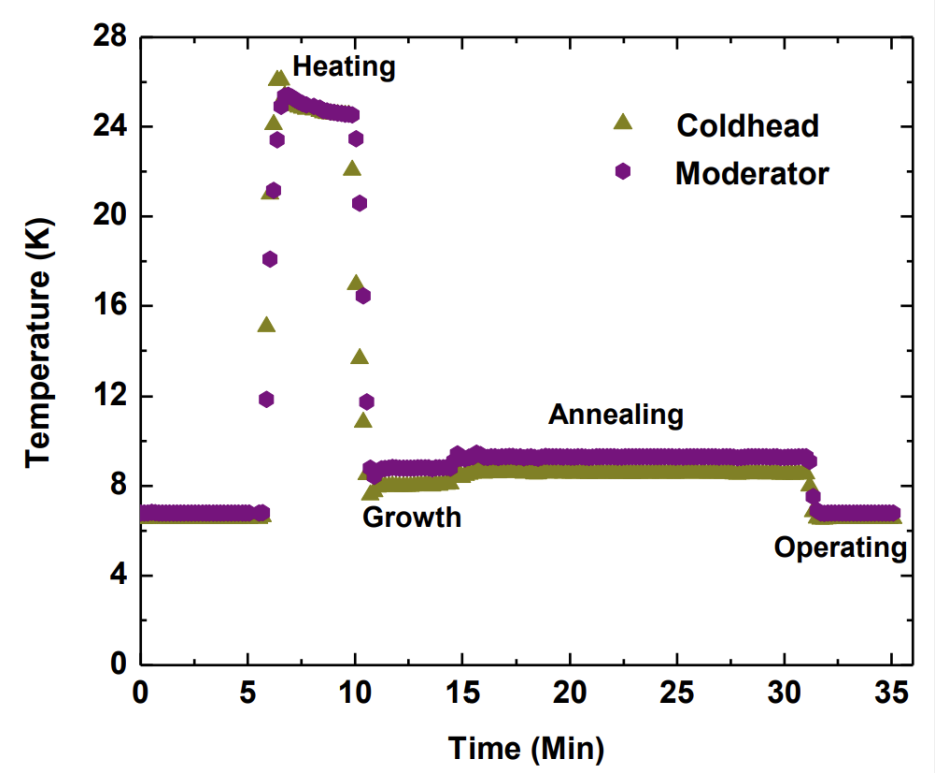

Figure 2.4: Growth process of the rare gas moderator. [23]

6. Purge the neon gas feed line by opening the neon bypass valve.

7. Switch off the ion pump

8. Open the neon valve and admit neon at a rate of 3sccm. Close the neon bypass valve and wait for 3 minutes

9. Switch off the neon gas feed, and close the neon valve. Anneal at 9.3K for 30 minutes.

10. Set the temperature to 6.8K and switch on the ion pump

A graph of the temperature throughout this process can be seen in figure 2.4.

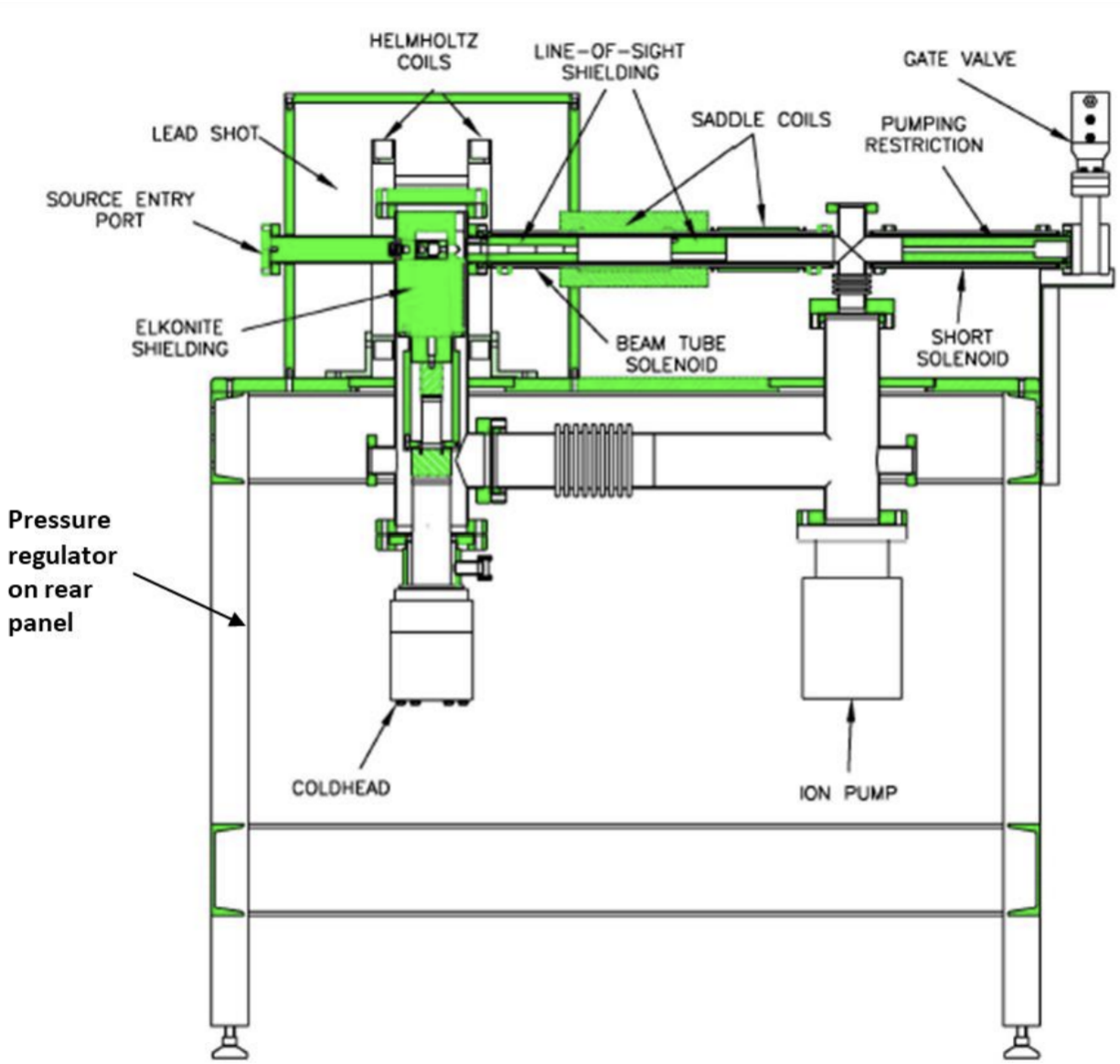

Figure 2.5: Diagram of the RGM system. [28]

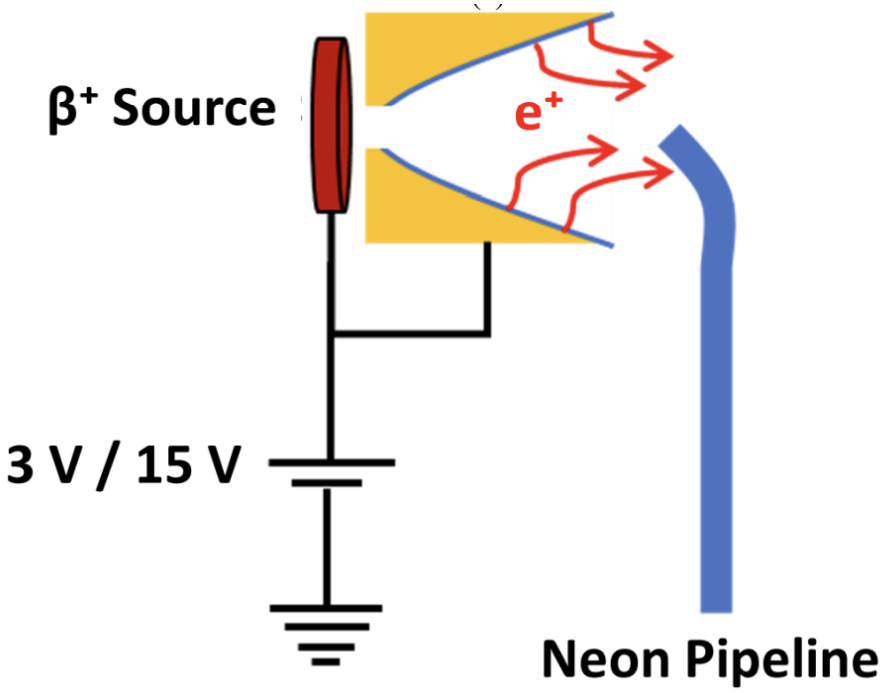

Figure 2.6: Rough sketch of the source capsule and moderator's cold head. [23]

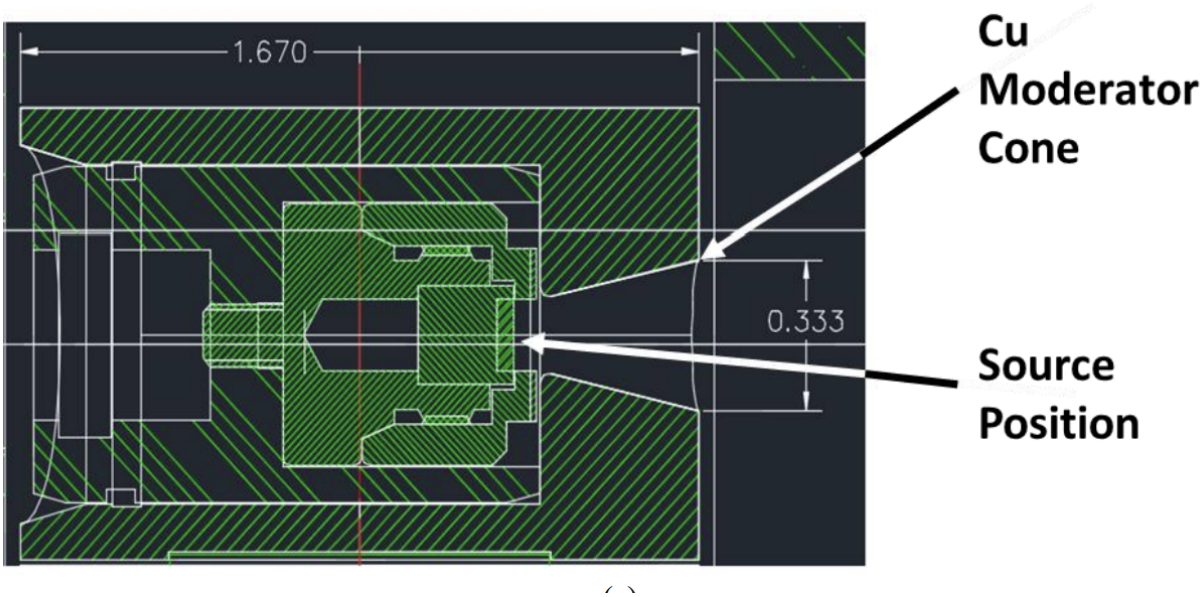

Figure 2.7: Schematic of the source chamber and moderator. [23]

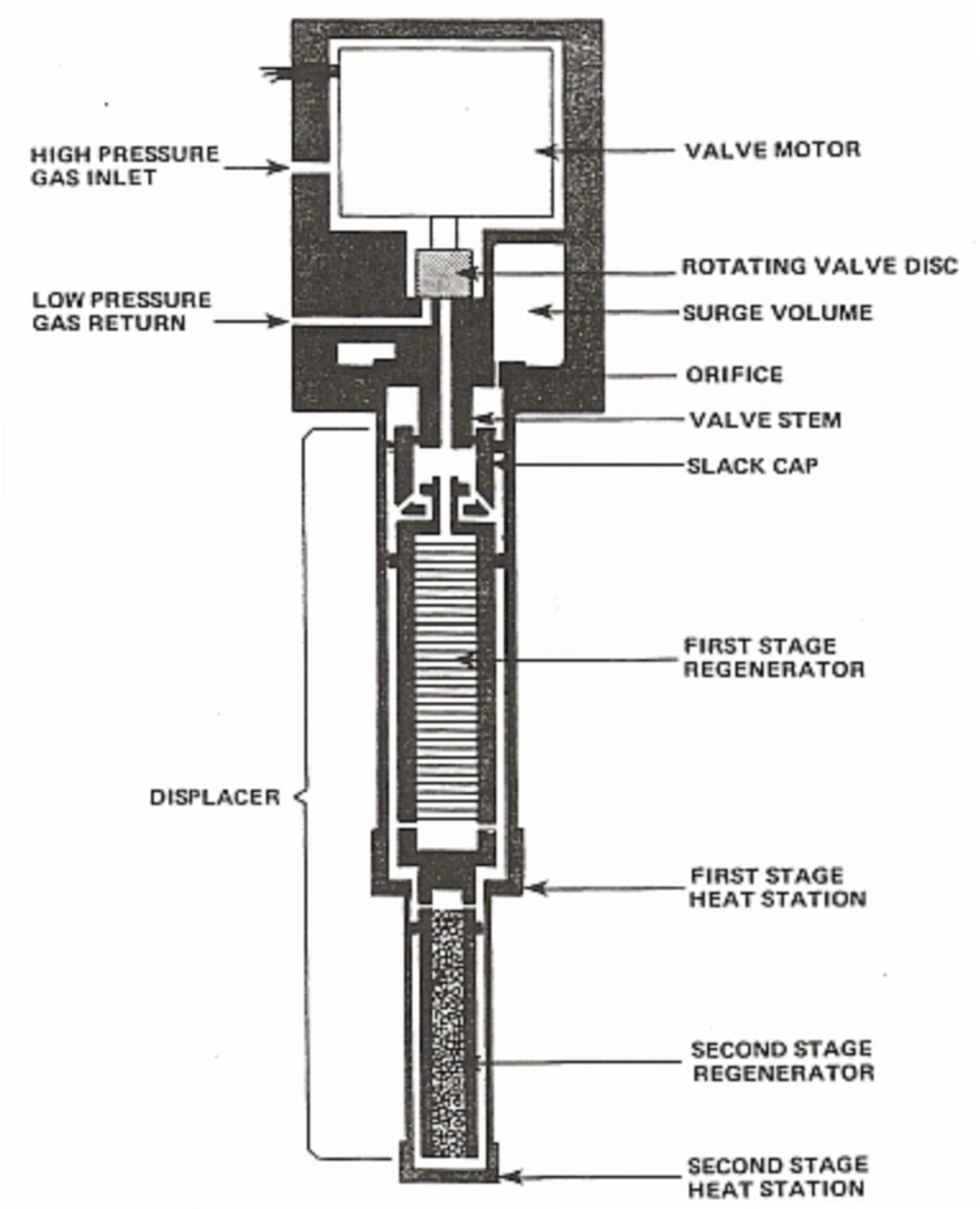

Figure 2.8: Diagram of the expander assembly. The entire Gifford-McMahon cycle takes place within this unit. [28]

The part of this assembly which produces the cryogenic temperatures is referred to as the expander (figure 2.8). The expander has two gas lines: one to receive high pressure helium from the compressor, and one to return the low pressure helium at the end of the cycle. It also has a connector which supplies electrical power from the custom power supply. The expander operates on the principle of the Gifford-McMahon refrigeration cycle (GM cycle), which is frequently employed in the design of cryocoolers. The expander works in 4 primary stages. First, the rotary valve opens to admit high-pressure helium from the valve motor housing into the expansion space. Once the helium has filled the expansion space, it begins to push against the displacer, which moves up, allowing the helium gas to expand and cool. The rotary valve then rotates to allow the helium to flow out of the expansion space, taking with it the heat from the system. Finally, the displacer returns to its original position, and the cycle begins again.[28]

The displacer assembly consists of two different stages. The second stage is smaller in diameter, is coupled to the first stage at the first stage heat station, and is the coldest part of the assembly. Each of these stages has internal regenerative heat exchangers, which serve to minimize the temperature achieved at the second stage heat station. The second stage is housed within a radiant heat shield and a vacuum shroud, and the sample holder is attached to the end of the second stage heat station.

The Ne gas required for the RGM to function properly must be at least 99.999% purity to produce a high-quality moderator, and is supplied by a pressure regulator and a mass flow controller. The pressure regulator is controlled manually, while the mass flow controller is controlled automatically by LabView. The pressure regulator requires a minimum of 10psi before the moderator growth process is able to proceed successfully. The neon gas feed line runs along the displacer assembly, up to the copper cold head, and points directly at the cold head.

The 6.8K achieved by the cold head, which is required in order to freeze Ne, is also cold enough to freeze most other common gasses. Because of this, the cold head will progressively

become contaminated by material other than Ne which freezes onto the cold head. Because these materials almost always have a freezing point which is higher than the 23K achieved when the old Ne moderator is warmed and blown off, these contaminants will persist until the cold head is warmed beyond their freezing point. In accordance with this, it's useful to occasionally allow the cold head to come up to room temperature so that the contaminants can be pumped out by the vacuum pumps which are connected to the RGM system.

The compressor used to supply the expander with high-pressure helium is the ARS-4HW. It has helium supply and return lines which connect to the expander, a power cable which draws from mains power, a cable which supplies power to the expander, and water supply and discharge lines for the internal water cooling system. It operates at 240psi, and comes pre-charged at this pressure from ARS, as do the high-pressure helium lines. The compressor also has an oil circuit to provide lubrication for the compression cycles. Because the oil and helium can come into contact during this process, the compressor also has an oil separator followed by an oil adsorber. After 12,000 hours, this oil adsorber is required to be replaced to ensure oil doesn't contaminate the helium lines and become introduced into the expander. This would cause the cryogenic system to become ineffective, if not inoperable.

2.2 Charged Particle Optics

The charged particle optics system can be divided into two primary categories: the electric-field-generating components and the magnetic-field-generating components (see figures 2.9 and 2.10). The magnetic field components are composed almost entirely of Helmholtz coils which are oriented co-axially with respect to the beam. There exist two sets of saddle coils within the RGM system, which serve as positron energy filters, and a permanent magnet situated directly behind the sample, which acts to focus the beam at the sample. The beam is also surrounded by 6 transverse magnetic field coils which serve to correct for the external magnetic fields which may affect the beam. The electric components include ExB

plates, which deflect the beam around various obstructions situated within the beam's path (namely a micro-channel plate which is used to collect Auger data), a time-of-flight (ToF) tube which assists in Auger electron collection, and a high-voltage electrode behind the sample, which is used to accelerate the positrons as they approach the sample in order to conduct measurements at higher positron energies.

To produce the axial magnetic field, we use a series of 18 Helmholtz coils, labeled 5 through 22. Each of these coils is powered by their own power supply, and their current values are shown in table 2.1.

Coil Number	Current Value (A)
5	4.20
6,7	6.15
8-12	4.00
13-18	4.23
19	4.25
20	4.20
21,22	3.80

Table 2.1: Current values for the coils. These values were found to yield the highest count rate at the sample.

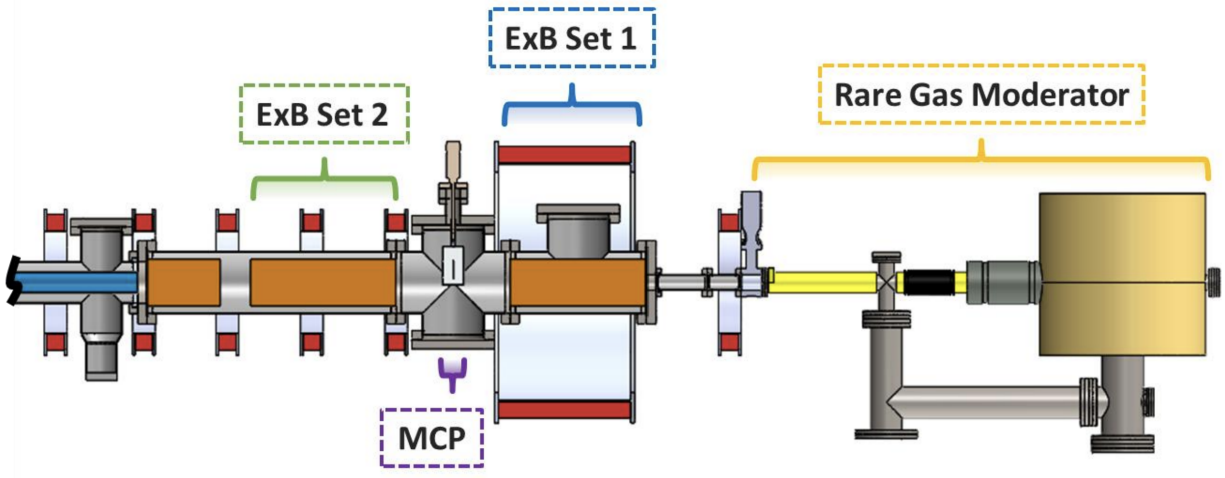

Figure 2.9: Right side of the beamline, including the RGM and MCP. [23]

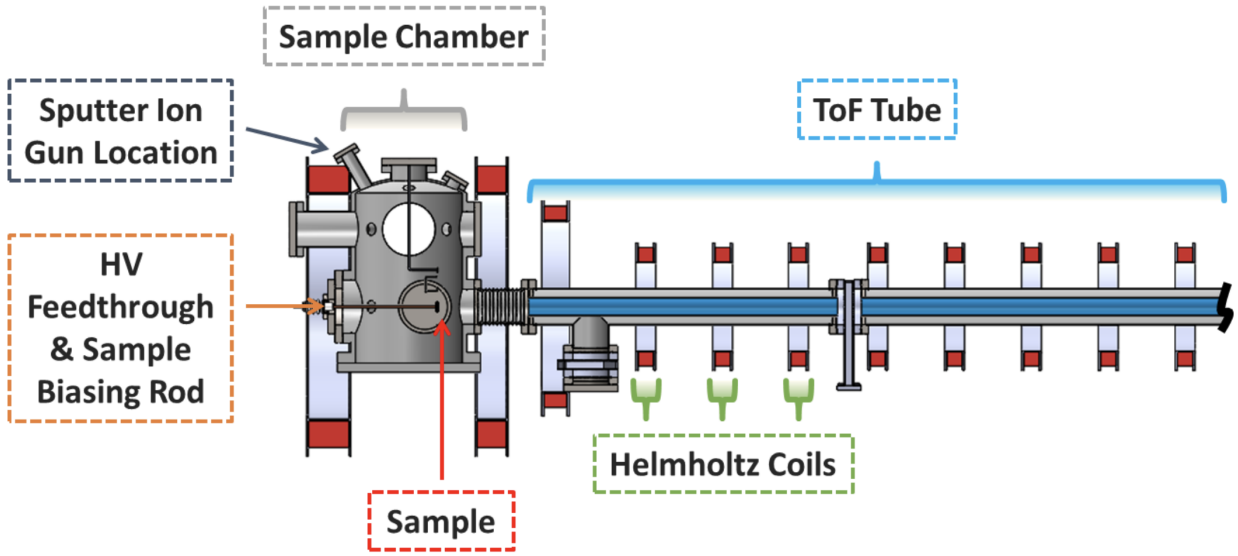

Figure 2.10: Left side of the beamline, including the vacuum system and sample chamber. [23]

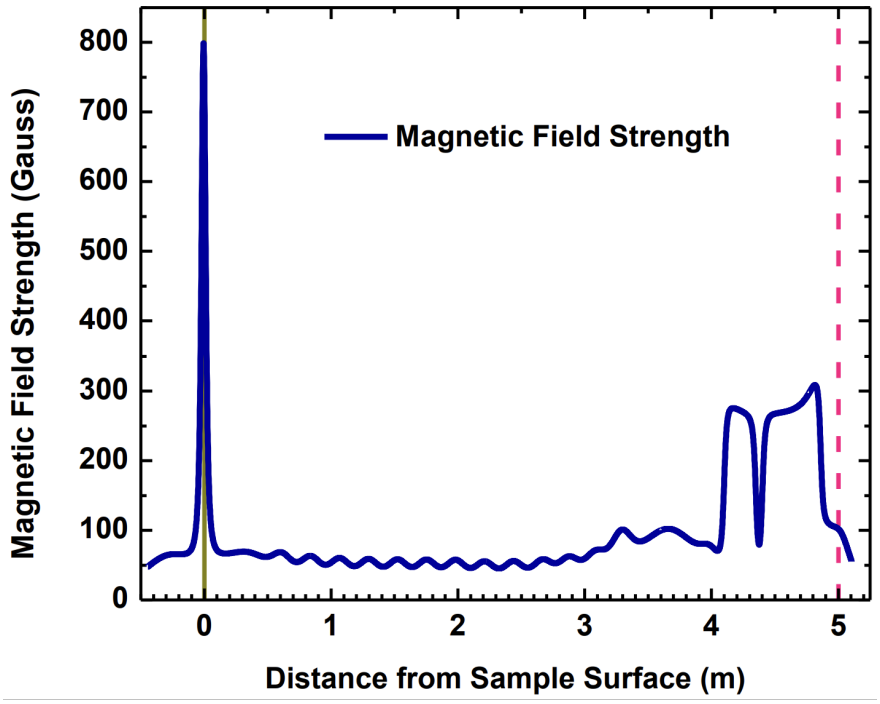

Figure 2.11: Simulated magnetic field strength in the center of the beam. [23]

We begin our labeling of these coils at 5 to account for the 5 coils which exist within the RGM system. These coils produce an average magnetic strength of 50 Gauss in the center of the beam (figure 2.11). This axial field serves to confine the particles, and ensure that they're guided down the center of the beamline without making contact with the walls. As they travel the length of the beam, the positrons will tend to spiral around the magnetic field lines due to the Lorentz force, which causes the component of the positron's velocity which is perpendicular to the beamline to rotate at a constant rate, while the velocity component parallel to the beam remains unchanged.

The saddle coils contained within the RGM system, shown in figure 2.12, are situated perpendicular to the beamline, and act to add a vertical component to the magnetic field within this region. This vertical magnetic field component, combined with a tungsten shield, serves to act as a filter for the positrons coming from the moderator. Only positrons whose velocities are low enough such that they can be sufficiently deflected so as to avoid the tungsten filter will make their way further down the beamline.

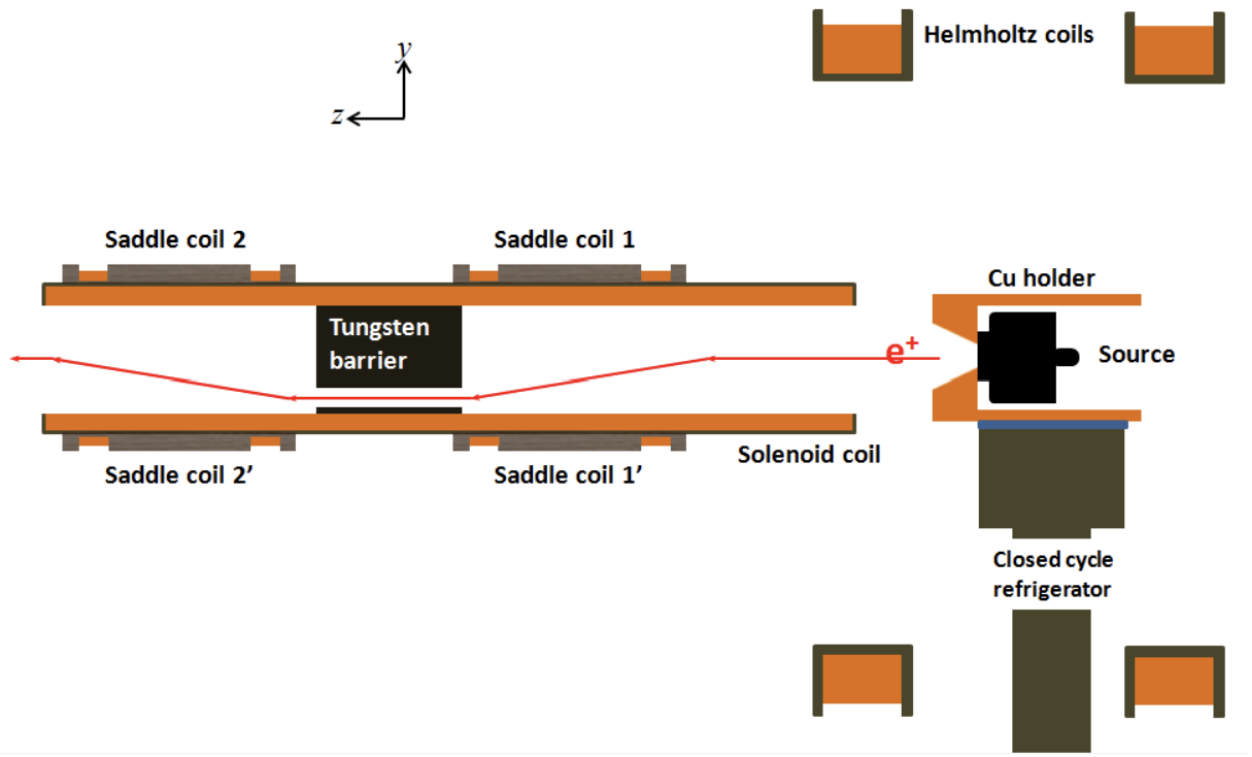

Figure 2.12: Tungsten shield used to filter positrons energies. [23]

The transverse coils are divided into three sections which, together, run the entire length of the beam, and serve to cancel out any magnetic field present within the environment surrounding the beam. Their current values are shown in table 2.2.

Coil Section	Horizontal Current Value (A)	Vertical Current Value (A)
1	-2.75	-1.00
3	-1.00	-0.90
3	-2.00	-2.00

Table 2.2: Current values for the transverse ambient-field correction coils.

Within the beam's path, there is situated a micro-channel plate (MCP), which is used to collect Auger electrons for PAES experiments. To avoid the positrons colliding with the back of the MCP, and to ensure the Auger electrons emitted from the sample can be collected, we use two sets of ExB plates; one on either side of the MCP. A third pair of plates exist, but these aren't necessary, and remain grounded for the current experiments. These plates are constructed from two parallel plates made of stainless steel placed 1.05" apart, with a

10.171" gap between the two sets of plates where the MCP is situated. There is another 3" gap between the second set of plates and the third (grounded) set. The terminals for these electrodes stick directly out of the sides of the beam, and by applying a bias to these terminals we generate a uniform electric field between the plates which is perpendicular to the axial magnetic field. The magnitude of the deflection of the positrons can be predicted using the following equation

$$\Delta y = \frac{(V_2 - V_1)L}{2dB}\sqrt{\frac{m_p}{2[E_k - q_p(\frac{V_2-V_1}{2})]}} \tag{2.1}$$

Here, Δy is the vertical displacement of the electron (see figure 2.13), $(V_2 - V_1)$ is the bias applied between the plates, L is the length of the plates, d is the distance between them, B is the magnitude of the magnetic field, m_p is the mass of the positron, E_k is the positron's kinetic energy, and q_p is the charge of the positron.

ExB Section	South Plate Bias (V)	North Plate Bias (V)
1	0.0	-85.0
2	+27.3	-25.1

Table 2.3: Bias values for the ExB plates. ExB set 3 remains grounded.

In the experiments conducted in this thesis, we are concerned only with Doppler broadening experiments, which requires only gamma ray data. We left the MCP disconnected, and were concerned only with the ExB plates' ability to deflect the positrons around the MCP; we were unconcerned with collecting Auger electrons.

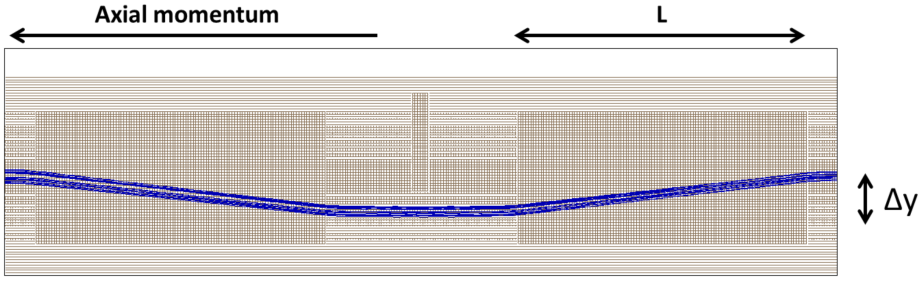

Figure 2.13: Simulated deflection of the positrons caused by the ExB plates. The MCP can be seen between the plates. [23]

The ToF tube, which runs most of the length of the beam between the ExB plates and the sample chamber, serves two primary purposes. The bias applied to the ToF tube can decelerate high-energy Auger electrons emitted from the sample, causing their time-of-flight to be greater, which enables a higher resolution of the collected data. The ToF tube also serves to provide a region free of electric fields which may serve to deflect the electrons (and positrons) off of their intended flight path. Again, because we were concerned only with gamma ray data, the effects of the ToF tube were mostly irrelevant for our purposes, and the ToF tube remained grounded. In this way, it doesn't interfere with the kinetic energies of the positrons while still providing a field-free region.

The positrons are focused at the sample by way of a permanent magnet situated behind the sample holder. As the magnetic field intensity increases, the magnetic field lines which are followed by the positrons begin to tighten, causing the beam to become more narrow as it falls within the region of higher magnetic flux (figure 2.14). This effect is characterized by the ratio of the magnetic field strength far from the sample to the field strength at the sample's surface.[29]

$$\frac{r}{r_0} = \sqrt{\frac{B_0}{B}} \tag{2.2}$$

Here, r_0 and B_0 denote the cyclotron radius and magnetic field strength at the surface of the sample, while r and B denote these same values far from the sample. The magnet used for this purpose was purchased from CMS Magnetics. It is 1" in diameter and 3/8" in thickness. The magnet is made of a SmCo alloy, which has a Curie temperature (700C to 800C) which is far higher than that of other rare earth magnets, such as Nd (310C to 400C). This difference in Curie temperatures is essential for our purposes, as annealing the samples using the heater attached to the sample holder can cause the magnet to reach temperatures exceeding 500C.

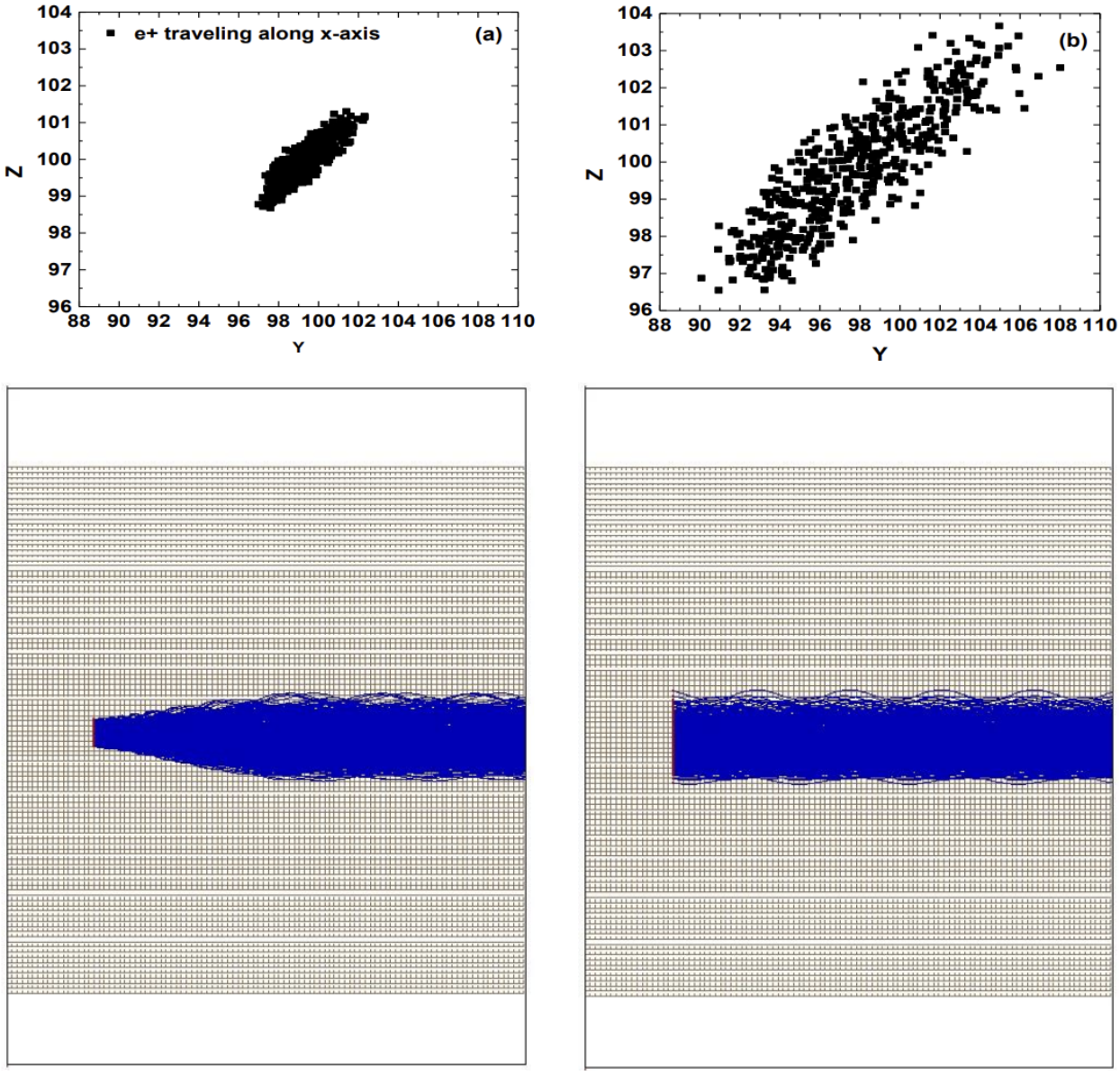

Figure 2.14: Simulated positron trajectories with (left) and without (right) the sample magnet in place. [23]

2.3 UHV System

The entire beamline is maintained at ultra-high-vacuum pressures. At the time of writing this thesis, the RGM is held at 10^{-9} torr, while the rest of the beamline is held only at 10^{-8} torr. One of the primary motivations for maintaining UHV pressures is to maintain a clean sample. At (relatively) higher pressures, contaminants from the environment will become coated on the surface of the sample, and can noticeably degrade the quality of the collected data. This is mainly a concern in PAES experiments, which are extremely sensitive to the chemical composition at the surface of the sample. For Doppler broadening experiments, this is less of a concern, and the UHV serves primarily to maintain beam intensity; gas molecules present within the beamline can cause positrons to scatter into the walls, thereby reducing the brightness of the beam. The UHV pressures in the RGM are more important. As mentioned previously, the cryogenic temperatures present at the moderator cause the cold head to accumulate contaminants over time. A pressure on the order of 10^{-9} torr helps to mitigate this effect, and extends the time between maintenance shutdowns.

The UHV system is composed of a number of different vacuum pumps which work together to achieve the desired pressures, each of which operates within a different pressure regime. This system is also divided into two main parts: the beam side (shown in figure 2.15) and the RGM side. The RGM side is an automated self-contained system, which is operated via the same LabView control program as the moderator. It consists of a Pfeiffer HiCube turbo/diaphragm pump station which handles the roughing of the system, and a 100 L/s TiTan Gamma Vacuum ion pump which is used to push the RGM to the UHV regime after roughing has been completed. The pressure in the RGM is measured by a RPT200 for the range of atmospheric pressure to 10^{-4} torr, and a HTP200 for pressures within the range of 10^{-3} to 10^{-9} torr. The beam side roughing is accomplished by a Pfeiffer Balzers TPU-170 170 L/s turbo pump, which is backed by an Agilent dry scroll pump. To push the beam-side volume from the roughing pressure to the UHV regime, a Perkin-Elmer TNB-X 1001886 200 L/s ion pump is used. Additionally, the sample chamber is equipped with a

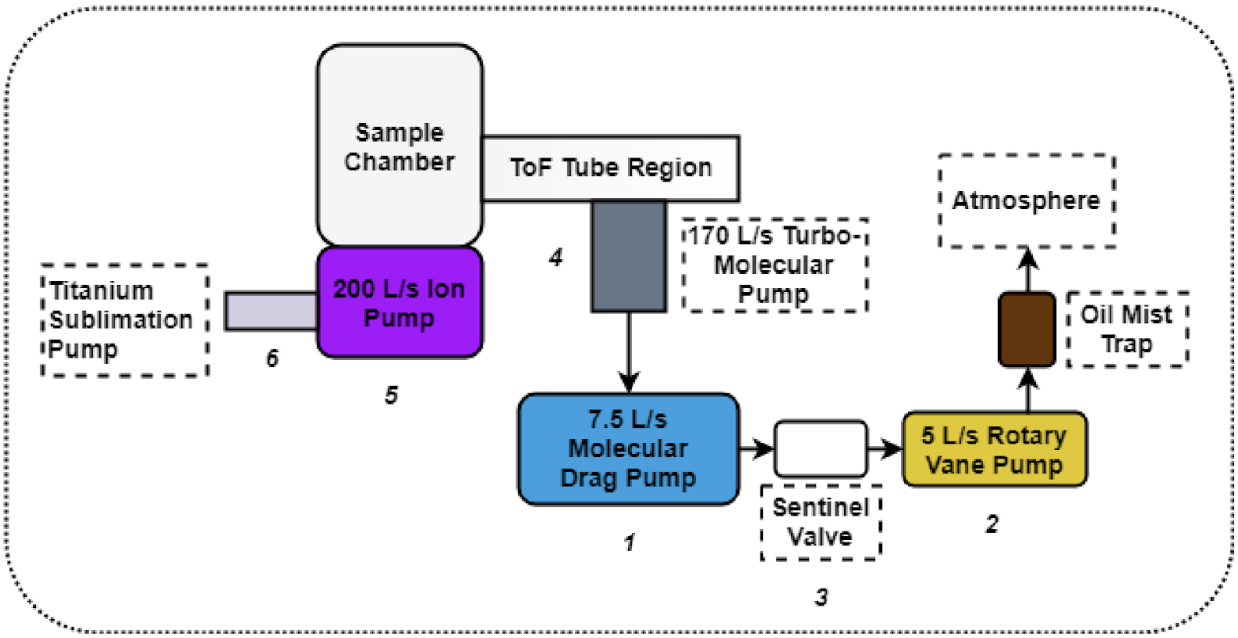

Figure 2.15: Diagram of the sample chamber UHV system. [23]

titanium sublimation pump (TSP) and cold trap. The ion pump and TSP are controlled by a Perkin-Elmer Digitel 500 model 222-0400 and a Perkin-Elmer model 224-0540, respectively.

There also exist two gate valves along the path of the beam which serve to isolate sections of the beam; one between the vacuum system of the sample chamber and the MCP area, and another between the MCP area and the RGM. The RGM gate valve is a manual screw-type gate valve, while the gate valve between the sample chamber and the MCP area is an electro-pneumatic valve.

Bringing the chamber (and, in general, the entire beamline) back down to UHV from atmospheric pressure is a frequent occurrence, as it follows every sample change, and can either be trivially simple or frustratingly complex depending on the environment within the system. Ideally, the procedure is as follows: Start the Agilent Dry Scroll pump to ensure nothing gets pushed back into the system when the gate valve is opened, open the gate valve between the turbo/roughing pump and the chamber, start the turbo pump, then start the ion pump. This should bring the system down to the necessary pressure, although the titanium sublimation pump may need to be used to achieve the last order of magnitude. To

do this, we simply operate the Perkin-Elmer TSP controller, selecting each filament in series, applying a current of 40 amps until the pressure rises and stabilizes, then switching off the TSP and allowing the pressure to drop before switching to the next filament and repeating the procedure.

If this procedure is unable to achieve the desired pressure, it may be necessary to bake the chamber. There exist strips of resistive heating tape which envelop the chamber. To bake the chamber, we connect each of these tapes to a variable resistor, and adjust the resistor to draw the desired current (usually around 2A). It is important that these tapes be connected in such a way that you never draw more current from a given circuit breaker than the breaker is rated for. Not only is this a safety hazard, it will also cause the breaker to trip, halting the baking procedure. Once all of the tapes have been connected and brought up to their defined current, the chamber should be allowed to bake for as long as necessary (usually only 2 days) before ending the bake. Before switching off the heating tapes, it's good practice to run the ion gun and TSP to outgas both of these systems. Once both of these have been run, the heating tapes can be turned off and disconnected, and the system allowed to cool to return to UHV.

2.4 Sample Chamber and Manipulator

The sample chamber houses the sample holder and manipulator assembly, an ion gun used to sputter the sample, a high voltage feedthrough with a sample biasing rod, one detector well on either side of the sample, and a viewport. A diagram of the sample chamber is shown in figures 2.16 and 2.17.

The sample holder is a stainless steel plate 1.65" in diameter, and has the sample mounted to it via two stainless steel brackets which are moved into place and fixed using two small screws. The holder is mounted to a stainless steel bracket using two 1.25" steatite standoffs. This assembly has a heater mounted to its back, which allows the sample to be annealed without removing it. The stainless steel bracket is mounted to the manipulator arm, which enables it to be translated along all three axes, and rotated about the roll and yaw axes.

The sample bias rod, which is situated directly behind the sample holder, is used to bias the sample to high voltage in order to enable high-energy experiments to be conducted. Currently, this bias rod is connected to a Bertan Series 230 30kV 0.400mA high-voltage supply by way of a high-voltage feedthrough. While the sample can be brought up to this voltage, it's essential that the arrangement of the components within the chamber be oriented such that the bias rod does not arc. This can be mitigated by achieving minimal pressures, as the breakdown voltage is proportional to the pressure within the chamber, governed by Paschen's law [30]

$$V_B = \frac{Bpd}{\ln(Apd) - \ln[\ln(1 + \frac{1}{\gamma_{se}})]} \tag{2.3}$$

Here, p is the pressure in pascals, d is the distance between the two electrodes, γ_{se} is the secondary electron emission coefficient, and A and B are experimentally determined constants which relate to the saturation ionization and excitation energies. For air with an E/p of 450 to 750V/(kPa·cm), these values are $A = 112.5(\text{kPa·cm})^{-1}$ and $B = 2737.5\text{V/(kPa·cm)}$.[31]

Because the energy of the positrons in this system is negligible (about 1eV), the energy of the positrons which hit the sample is effectively equal to the bias voltage in terms of eV (1kV bias yields 1keV positrons, 10kV yields 10keV, etc.). [32]

The ion gun which is mounted to the chamber is fixed such that the sample must be turned 180 degrees to face the rear of the chamber in order to be sputtered. The ion gun sputters the sample by ionizing argon gas which has been admitted to the chamber, and accelerating the argon ions across a potential gradient towards the sample. The bombardment of the sample by these argon ions slowly erodes the top atomic layers of the sample, so care must be taken if the sample under investigation contains sensitive thin films which are of interest. To sputter the sample, we first close the electro-pneumatic gate valve between the sample chamber and MCP region, and admit argon into the chamber by way of a leak valve, which allows precise control of the argon pressure within the chamber. Once the pressure in the sample chamber has been brought to 10^{-5} torr, we slightly open the gate valve to the turbo pump to bring the chamber into equilibrium at this pressure. We then switch on the ion gun, observe that the beam is visible and hitting the sample in the intended position, and allow the ion gun to sputter the sample for an amount of time determined by our needs (cleaning the sample, exposing new layers to the surface, etc.). Once sputtering has completed, we follow our regular procedure of bringing the chamber back down to UHV pressures which was detailed in the previous section. Because argon is a noble gas, baking is very rarely required after the sputtering procedure.

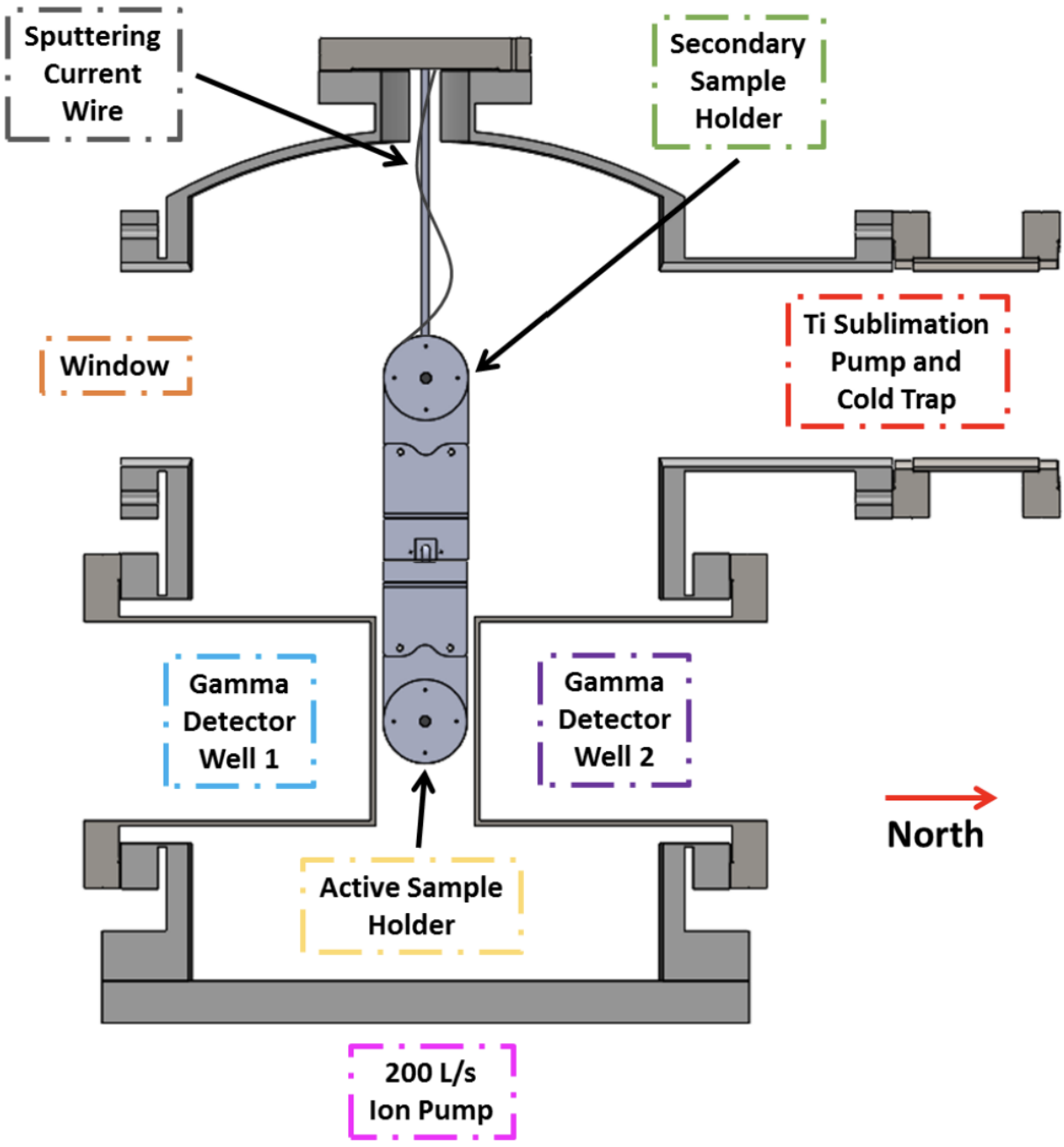

Figure 2.16: Front profile of the sample chamber. [23]

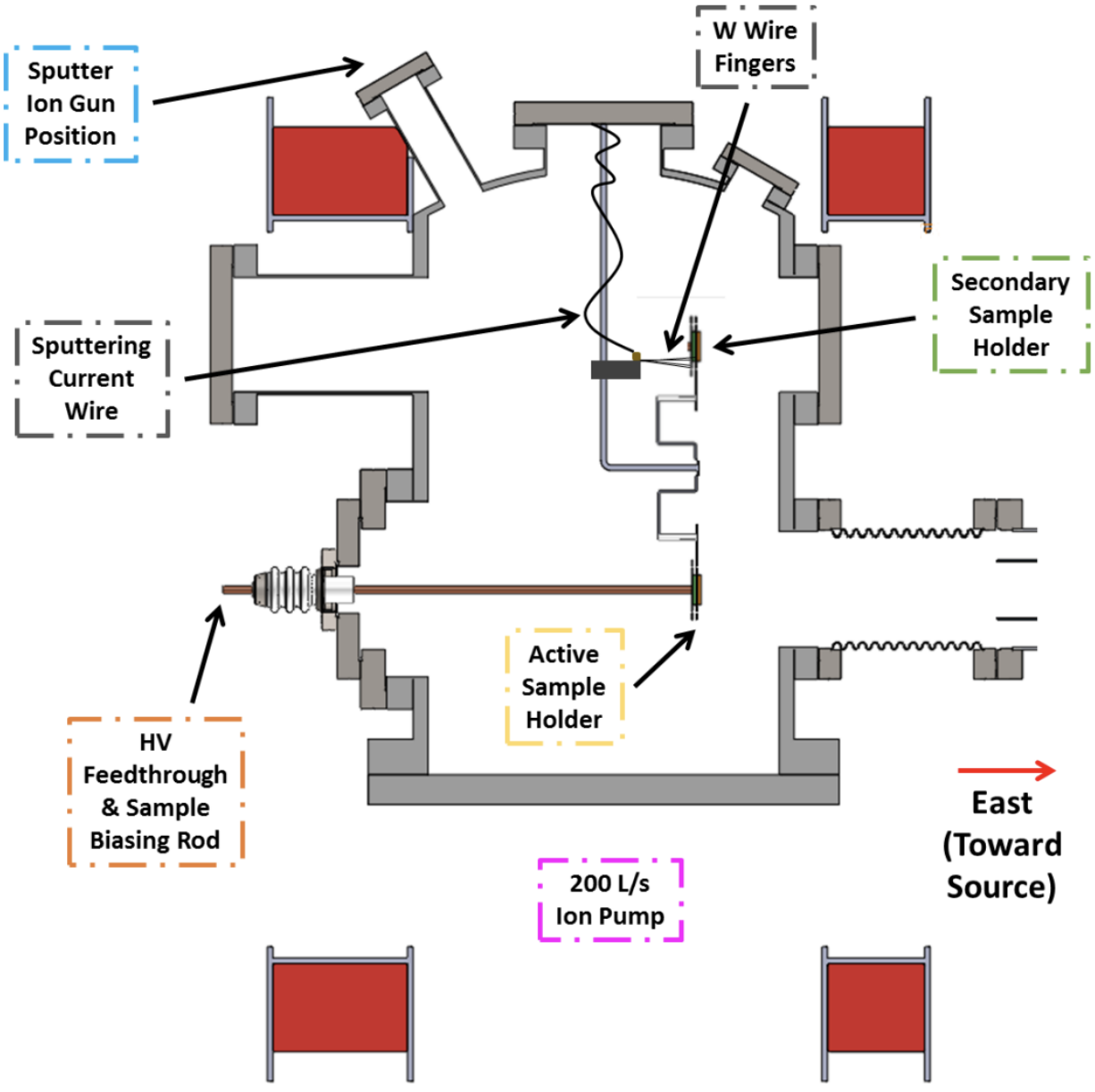

Figure 2.17: Side profile of the sample chamber. [23]

2.5 Detectors and Electronics

To collect our gamma ray spectra, we use two detectors. One sodium-iodide detector (NaI) and one high-purity germanium detector (HPGe). The NaI detector is composed of a NaI scintillation crystal, which employs a photomultiplier tube, and a voltage divider and high voltage decoupling circuit to produce an output signal. These detectors are useful for their high timing resolution, which is about 500ns at 511keV.[33, 34] In the experiments outlined in this thesis, the NaI detector was used only to confirm that the positrons were not hitting the walls of the chamber by setting up a coincidence condition between the two detectors. The HPGe detector was used to collect the spectra, as it has excellent energy resolution (about 0.3% at 511keV). The HPGe detector is constructed from a single crystal of lightly doped germanium. This crystal is surrounded by electrodes which apply a high voltage (3.5kV) across the crystal, causing electron-hole pairs created by the incident gamma rays to be migrated and detected at either end of the crystal. A simple sketch of the detector is shown in figure 2.18.

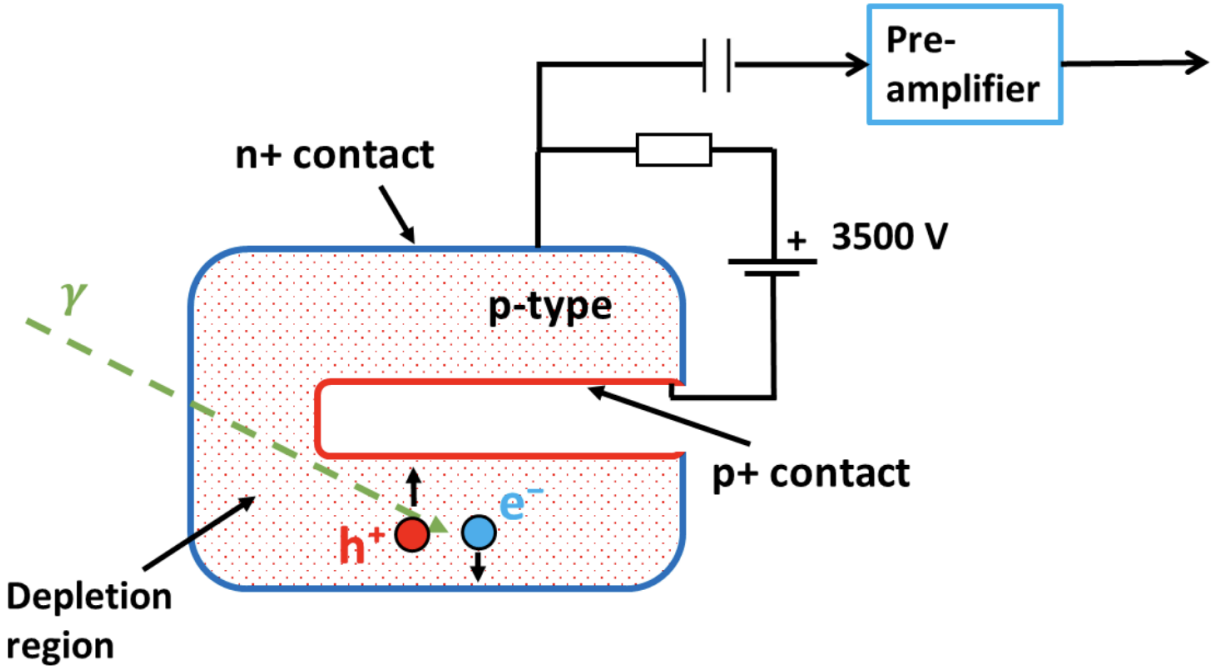

Figure 2.18: Simple sketch of the operating principle of the HPGe detector. [23]

Because this detector relies on electron-hole pair creation, thermal and vibrational noise effects can be considerable problems in achieving high-quality data. To mitigate these, the detector is kept cool by being partially submerged in a dewar of liquid nitrogen (figure 2.19), and sits atop a rubber mat which isolates the detector from vibration. The coincidence condition which is enabled by the NaI detector also serves to reduce the noise generated by this detector. One issue which is unavoidable in this detector is Compton scattering. Incomplete energy transfer from the incident gamma ray (figure 2.20) can cause the photon to scatter off of the lattice, generating an electron-hole pair which produces a signal resembling that of a lower-energy photon. This scattering process results in a great deal of noise in the region below the 511keV peak, but can be mitigated by the use of analog signal processing.

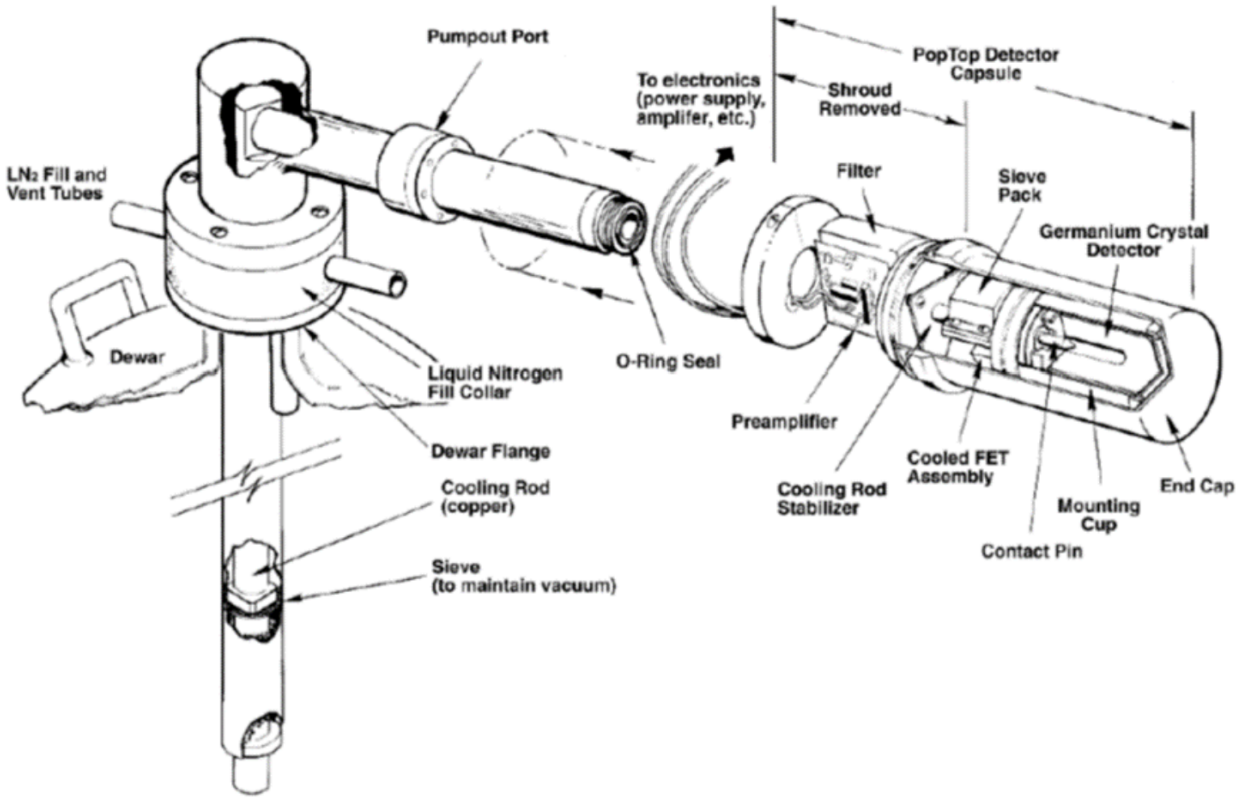

Figure 2.19: Schematic of the HPGe detector construction. [35]

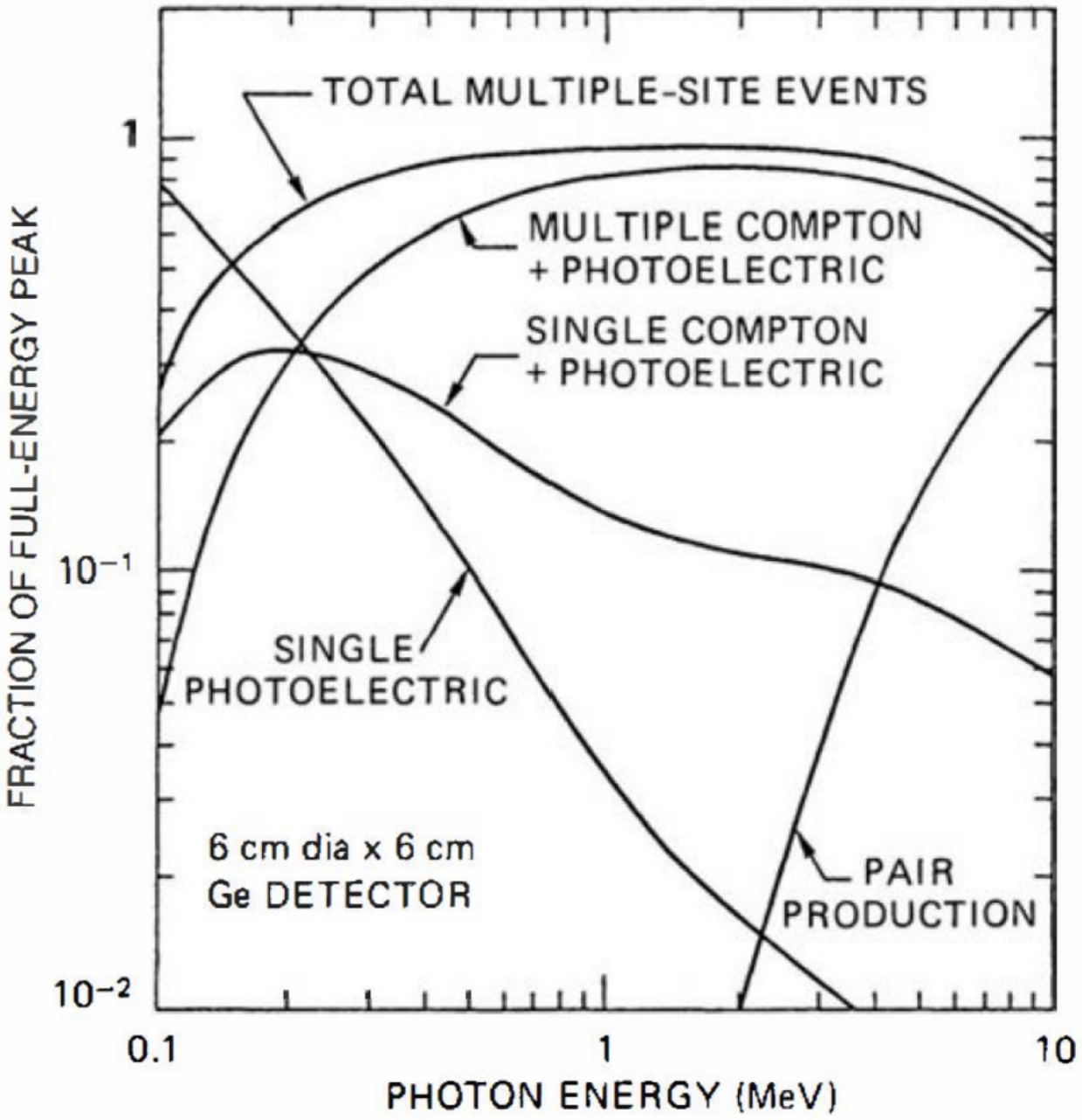

Figure 2.20: Fractional energy loss mechanisms within a HPGe detector. [36]

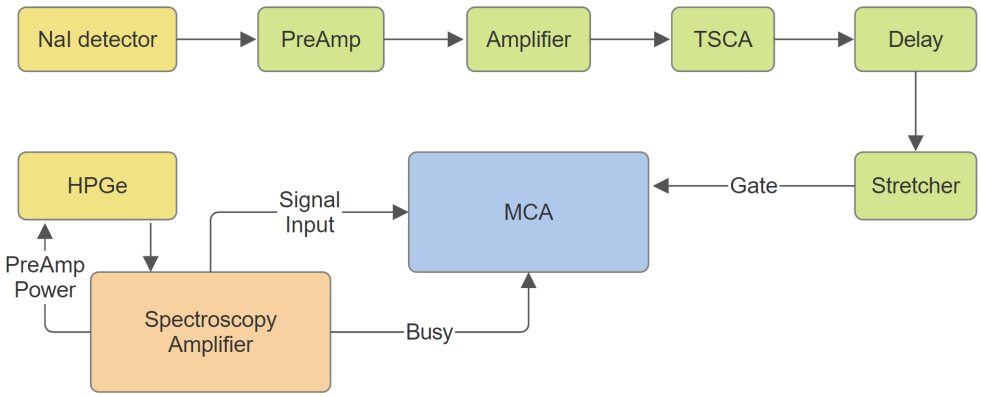

Figure 2.21: Block diagram of the analog signal processing and acquisition system.

To process these signals, we use a series of NIM (nuclear instrument module) units. The arrangement of these units is shown in figure 2.21, and the signal output from each of these electronic components is shown in figure 2.22. The HPGe detector circuit is simple. The detector output is fed into an Ortec 472a spectroscopy amplifier, whose output is sent to an Ortec multichannel analyzer (MCA). The MCA, which acts as an ADC, interfaces directly with the computer, which uses the Maestro software to collect and display the spectrum. The NaI detector runs a more complex circuit which is required to enable the coincidence condition. The output of the NaI detector is first sent to a Canberra model 2005 preamp and Sturrup signal amplifier, then through a Sturrup model 1435 timing single-channel analyzer (TSCA), an Ortec pulse delay, and then a custom-built pulse width extender before being passed into the "gate" input on the MCA. When the coincidence setting is enabled in Maestro, the MCA will only collect data when the "gate" input is active, rejecting any signal which arrives while the gate is low.

Both of these detectors require a high-voltage bias to operate. The NaI detector takes a bias of +500V, provided by a Bertan model 313B high voltage supply. The HPGe detector takes a bias of +3.5kV, provided by an Ortec model 660 dual 5kV bias supply. In addition to the high-voltage bias, the HPGe detector also requires the onboard preamp be provided power by the spectroscopy amplifier. If the preamp is unpowered, the high-voltage supply will remain shut down.

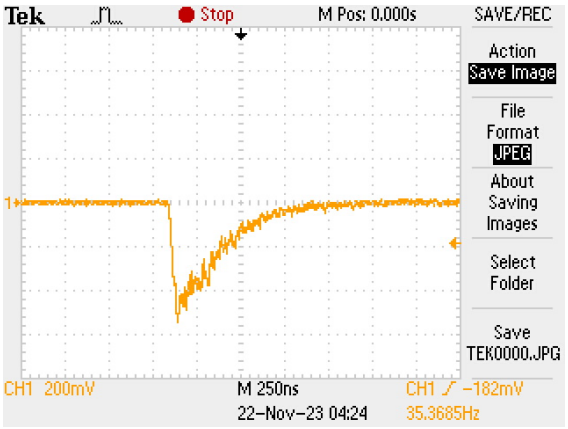

(a) NaI detector output

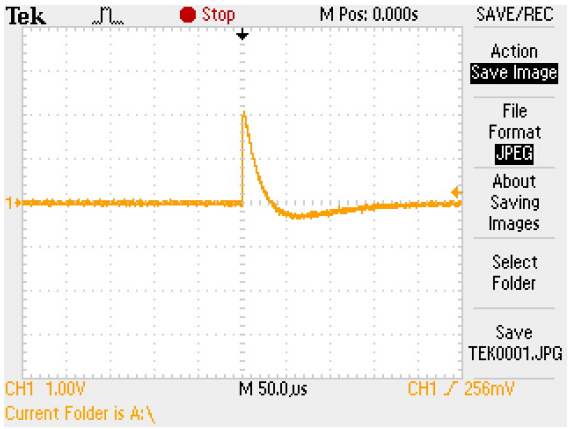

(b) NaI preamp output

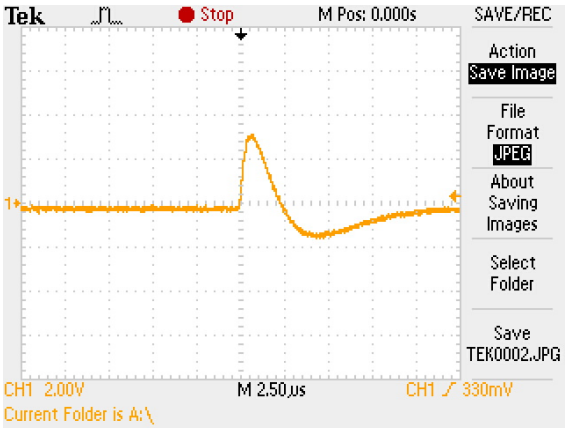

(c) NaI amplifier output

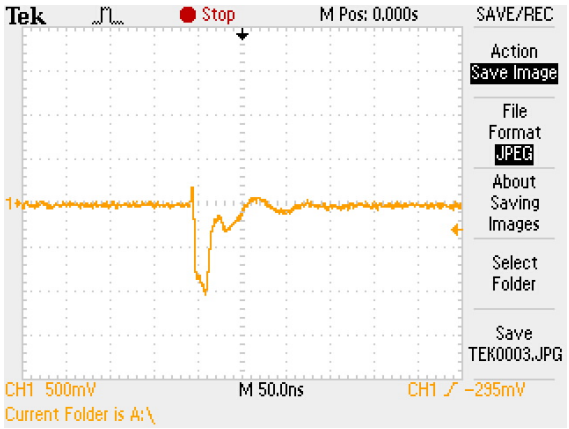

(d) TSCA output

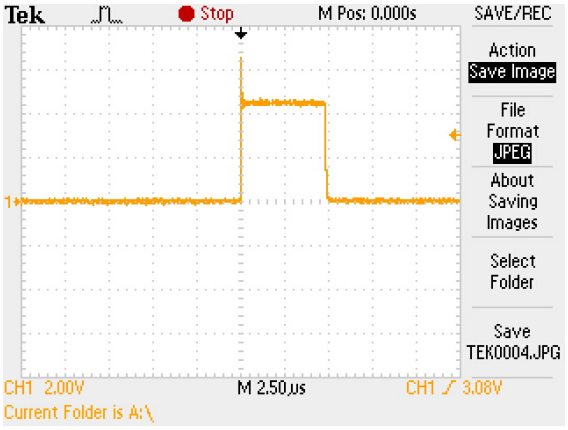

(e) Delay module output

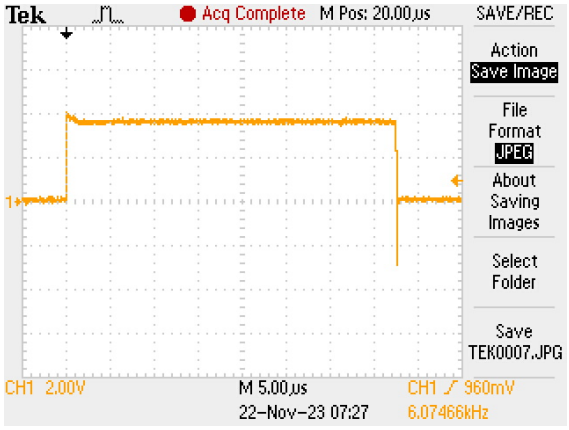

(f) Stretcher output

Figure 2.22: Analog signal processing steps for NaI coincidence condition.

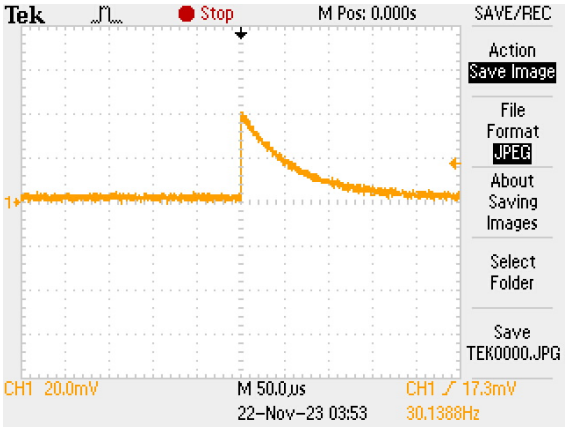

(g) HPGe output

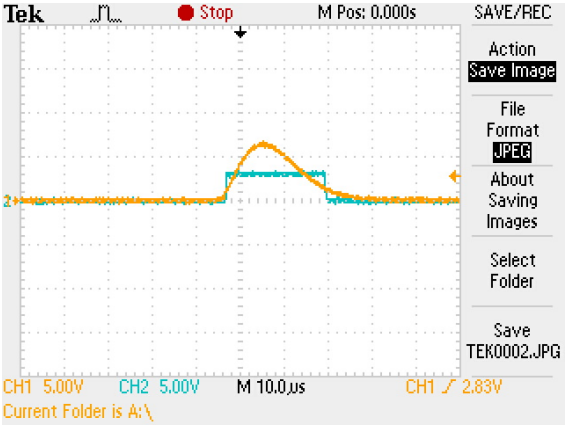

(h) Spectroscopy amplifier output (yellow) and the spec amp's busy signal (blue)

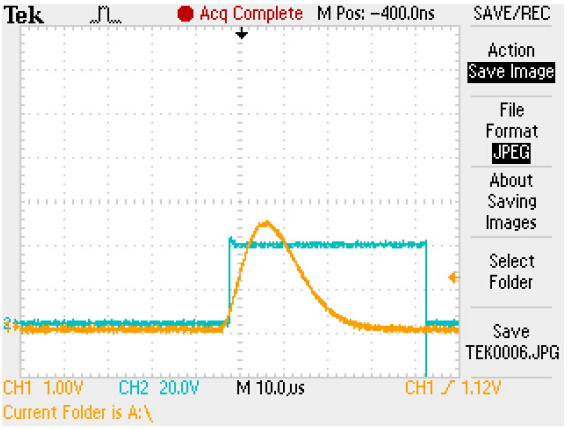

(i) Spectroscopy amplifier output (yellow) and the NaI coincidence condition (blue). The coincidence condition must be high to enable data acquisition.

Figure 2.22: Analog signal processing of the HPGe detector output

Chapter 3

Beamline Repairs and Upgrades

3.1 Coldhead Repairs

After returning from UTA's shutdown following the pandemic, we found that the beamline had become inoperable. When we tried to re-start the beam, the first issue we noticed was that the cold head was unable to maintain the 6.8K required to keep the moderator in working order. To solve this problem, we contacted the manufacturer, Advanced Research Systems (ARS) and requested their assistance in troubleshooting the issue. ARS advised that we remove the displacer assembly from the expander and ship it to them to be serviced.

The process of disassembling the expander and removing the displacer assembly is a delicate one, as the parts are precisely machined, and the displacer assembly is sensitive to moisture. In order to maintain the integrity of the displacer assembly, the entire procedure needed to be completed within an hour, and the displacer needed to be stored and shipped in two nested nitrogen-filled ziploc bags. To begin, we connected two vent fittings to the high-pressure helium line ports on the expander's valve motor housing. This assembly contains helium gas at 240psi, and must be vented slowly. Once the expander had been brought to atmospheric pressure, we loosened the 8 bolts on the bottom of the assembly, and carefully lowered the valve motor housing. The valve motor assembly and housing are not sensitive to

moisture, and were stored on a benchtop with a layer of tin foil covering the opening. Next, we used a custom displacer puller, which was provided by ARS, to remove the displacer assembly. The displacer fits tightly into its opening within the expander, and requires a small amount of force in order to be removed.

Upon removing the displacer, we discovered that the displacer was covered in oil, meaning the displacer would need extensive repairs before it would be operational again. The cause of this was a lack of maintenance of the adsorber within the compressor. The adsorber is responsible for ensuring that the oil used to lubricate the compressor does not enter the high-pressure helium line. It needs to be replaced after 12,000 hours of use, and we had missed this maintenance milestone due to being absent from the lab for an extended period. To remedy this, we would also have to return the compressor and valve motor assembly to ARS for repairs. It took a year for them to return these components to us in working order. In that time, we cleaned the expander housing using ethanol and isopropyl alcohol to ensure it was free of oil prior to receiving the repaired expander assembly. Figures 3.1 and 3.2 show the oil contamination in the valve motor assembly and displacer housing, respectively.

Once the assembly was returned to us, we re-assembled the system. We began with the displacer assembly which, as before, was required to be installed within one hour after opening the nitrogen-filled bag in which it was shipped. To begin the install, we inserted the displacer assembly into its place. Following that, we installed the rubber o-rings which seal the contact between the valve motor housing and the expander housing, then attached the valve motor housing and bolted it into place. Next, we connected the high-pressure helium lines to both the compressor and valve motor assembly, ensuring that the pressure equalized to the correct value of 240psi. We then connected the water lines, which act as coolant for both the compressor and the RGM solenoids, then routed power from the wall to the compressor, then to the valve motor assembly.

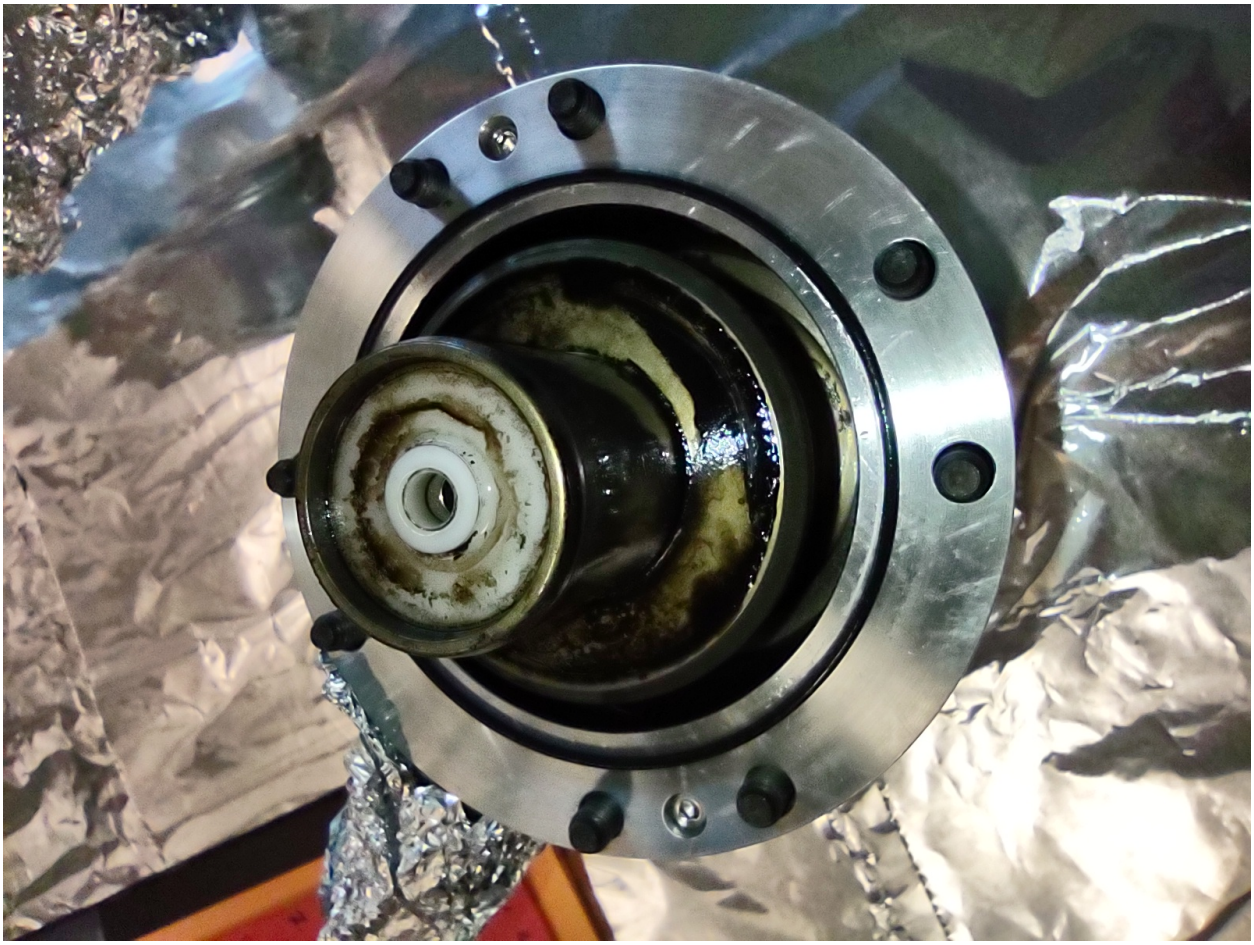

Figure 3.1: Valve motor assembly filled with oil, indicating failure of the helium compressor's adsorber.

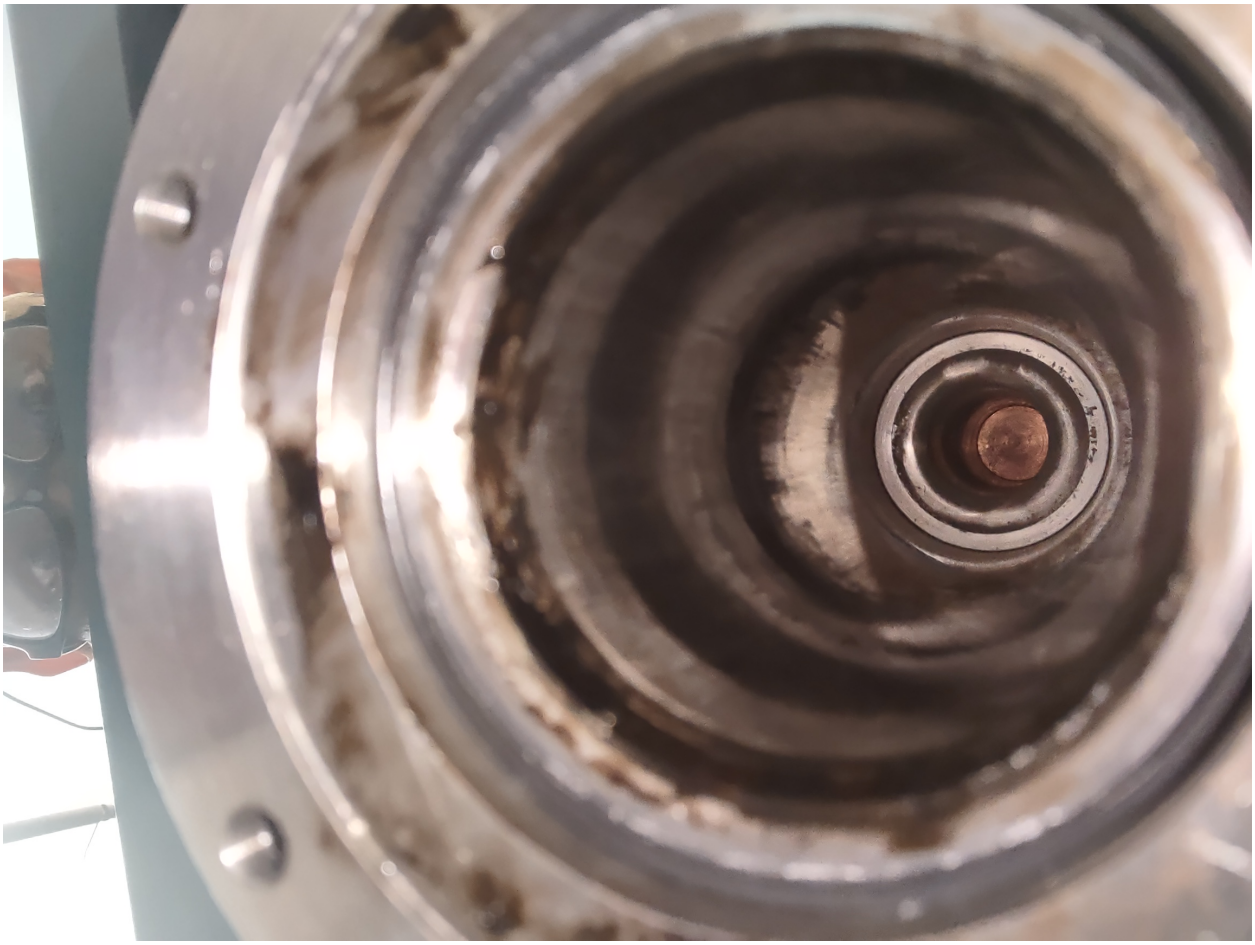

Figure 3.2: Inside of the displacer housing covered in oil.

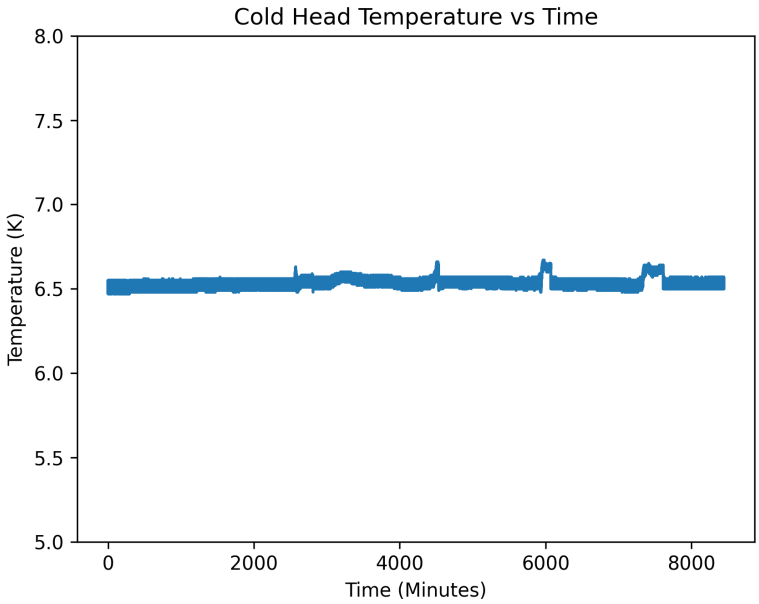

Figure 3.3: Cold head temperature remains stable around 6.5K over a period of approximately 5 days. Data was collected between August 10th and 15th, 2023.

The moderator takes approximately 7 hours to cool from room temperature to the 6.8K required for operation. Upon reaching 6.8K, the moderator was found the be stable and in working condition. After some time, the moderator temperature began to fluctuate, but this was determined to be caused by an excess of water flow to the cooling system, and upon reducing the flow rate the moderator temperature stabilized. Figure 3.4 shows the moderator holding a steady 6.8K with minimal fluctuations. Figure 3.3 shows the cold head holding a stable temperature of approximately 6.5K. Figure 3.5 shows the count rate from a NaI detector situated at the gate valve between the beamline region and RGM. The positrons are annihilating with the closed gate valve. To reach this location, the positrons must travel through the energy filter formed by the saddle coils and tungsten shield, meaning that only positrons whose energy has been sufficiently reduced will be seen by this detector. This count rate confirms that the moderator is working as intended.

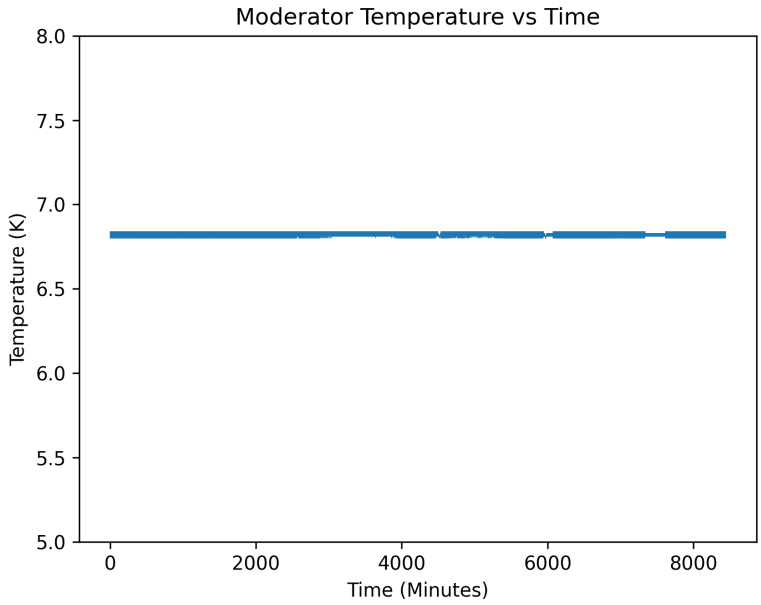

Figure 3.4: Moderator temperature maintaining a constant 6.8K over a period of approximately 5 days. Data was collected between August 10th and 15th, 2023.

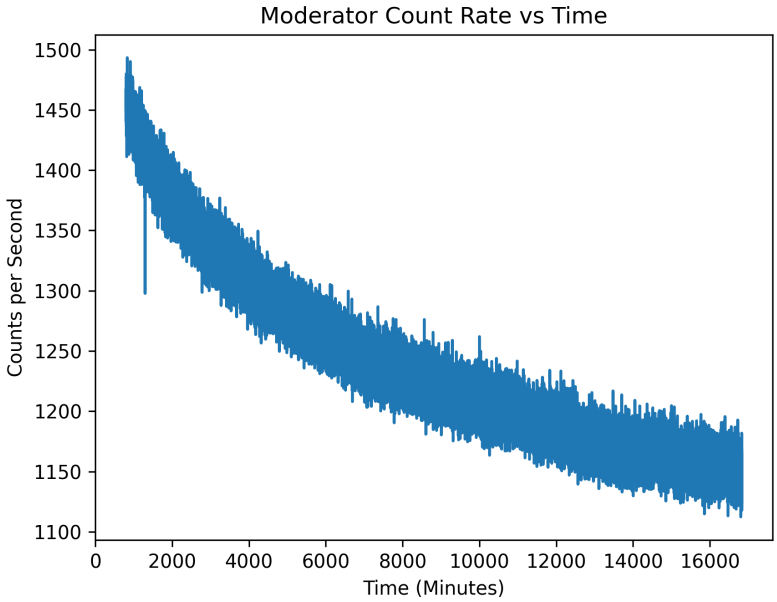

Figure 3.5: Gamma ray count rate at the RGM gate valve, showing that the moderator is operating as intended. Data was collected between August 10th and 21st, 2023.

3.2 Coincidence Measurement Optimization

During the course of these repairs on the CPB (Chemistry and Physics Building) beamline, the group also conducted experiments using another, nearly identical, beamline located in the Science Hall (SH). The only real difference between these two experiments is the moderator (which is a tungsten film in the SH beam) and the sample chamber / sample holder construction. The experiments being run in this beam required coincidence measurements, which record data only when the NaI and HPGe detectors receive simultaneous gamma rays. Because the gamma rays emitted from the positron-electron annihilation events are emitted at a 180 degree angle from each other, this ensures that only those gamma rays which come from positron annihilation events within the sample are collected in the spectrum.

To accomplish this requires a number of electronic modules. As detailed in the previous chapter, the NaI detector is first fed into a pre-amplifier and amplifier in order to produce a signal which is strong enough to be processed. From here, the signal is fed into the TSCA, which produces a timing signal based on the pulse height received from the NaI amplifier. This timing signal is then sent to a delay module, which produces a square pulse whose duration is dependant on the timing signal provided by the TSCA.

The problem which we found with this coincidence measurement was that the timing window produced by the delay module was too narrow. As a result, it was failing to measure counts which were from positron annihilation at the sample, thereby decreasing the count rate, and causing us to increase the collection time. This reduced the number of samples we could analyze during a given period, and made running experiments far more time-intensive. To remedy this, we designed and assembled circuits which act to lengthen the timing window, increasing the efficiency of our measurements, and lowering the time required to produce a spectrum.

These circuits, shown in figures 3.6 and 3.9, were constructed using the SN74121 monostable multivibrator with Schmitt triggers. This IC, which is produced by Texas Instruments, produces a square pulse which begins when the input (pin B) is pulled to a voltage greater

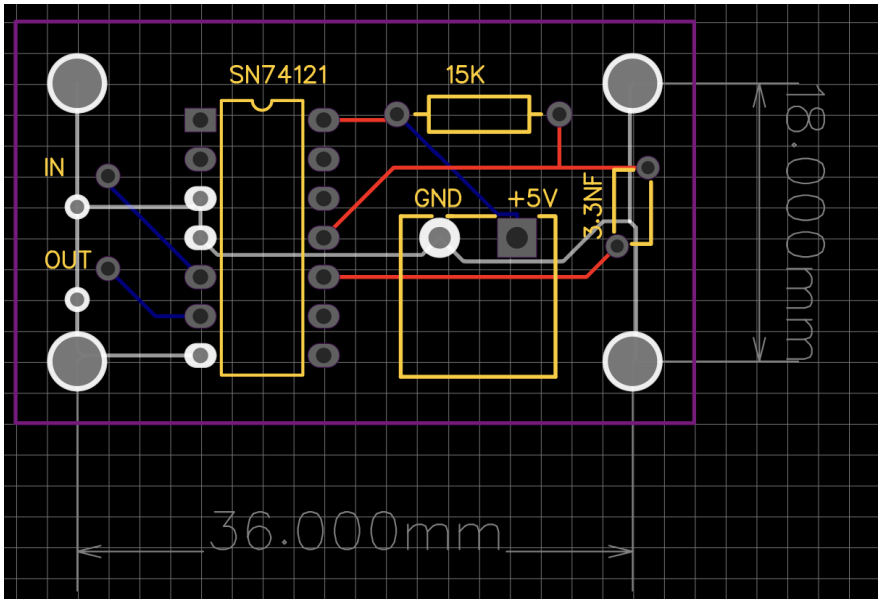

Figure 3.6: Wiring diagram of the stretcher circuit. Ground connections are highlighted in white.

than 1.55V, and lasts for a time defined by the external resistor and capacitor. The pulse time is calculated using the equation

$$t_{out} = C_{ext} R_{ext} \ln(2) \approx 0.7 C_{ext} R_{ext} \tag{3.1}$$

The positive-going pulse which comes from the delay module signals the Schmitt trigger to activate. Upon activation, the Schmitt trigger provides the necessary signal to the monostable multivibrator in order for it to produce the pulse of the defined duration. This negative-going pulse simultaneously pulls the base of the output transistor (bottom transistor in figure 3.8b) and the C_{ext} pin low, putting the circuit in its unstable state, and causing the output pin to go high. The capacitor then equalizes the charge between its plates at a rate which depends both on its capacitance value and the resistance value of the external resistor (equation 3.1). Once the capacitor has returned to equilibrium, and the circuit is back in its stable state, the base of the output transistor returns high, and the current flows through the transistor, turning off the output pin.

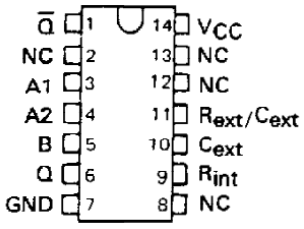

Figure 3.7: Pinout of the TI SN74121 monostable multivibrator IC.

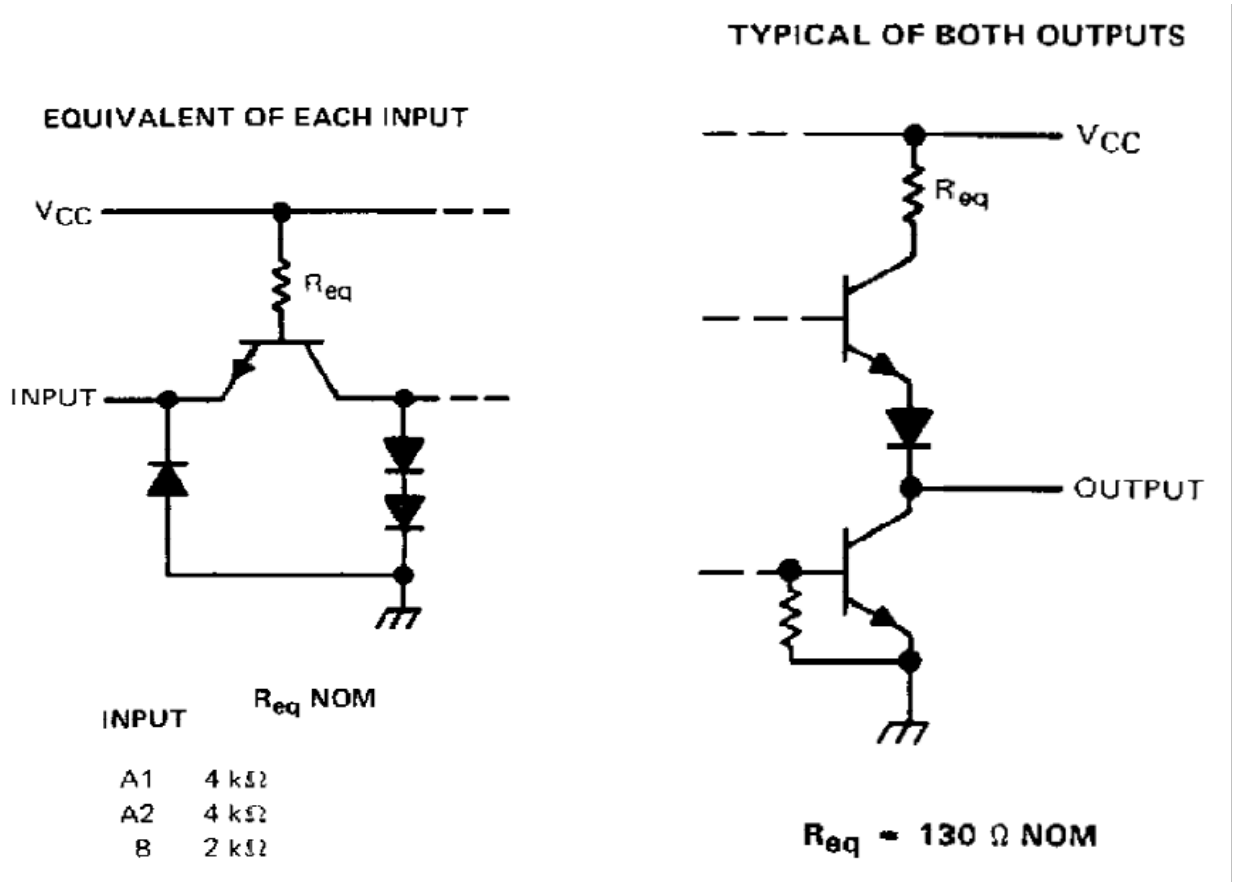

(a) SN74121 inputs

(b) SN74121 outputs

Figure 3.8: SN74121 inputs and outputs. Input comes from the Schmitt trigger - output comes from the collector of the bottom right transistor. The external capacitor and resistor are connected between these two diagrams.

In our case, we wanted to extend the pulse width to 35μs. To accomplish this, we used a 3.3nF capacitor and a 15kΩ resistor to yield a pulse width of $(0.7)(3.3\text{nF})(15\text{k}\Omega) = 34.7\mu$s. From figure 2.22f, we can see that the actual implementation of this circuit yields pulse duration of 38μs, likely due to slight variation in both the resistor and capacitor values. The circuit and PCB were designed using EasyEDA, and the components and PCB were ordered from LCSC and JLCPCB, respectively. The minimum order from JLCPCB was 5 units, so 5 of these circuits were ordered and assembled. These circuit's are fairly simple, and were soldered together in our lab.

We decided that the best way to house these circuits was to use an old NIM unit. We selected a module which had 10 BNC connectors on the front, which provided enough connectors for all 5 circuits to be housed within a single unit (each circuit requires two connections: an input and an output). The module was previously broken, so the old circuit board was removed to allow the new circuits to be mounted. The NIM unit has several terminals which supply power from the NIM bin to the module. While the NIM bin supplies $\pm$6V, $\pm$12V, and $\pm$24V, the circuits require 5V to operate. To accomplish this, all terminals were left disconnected except for the ground terminal and the +6V terminal. The 6V terminal was connected to a voltage regulator circuit set to provide 5V, which was connected to our pulse width stretcher to provide power to the circuit. The circuits are grounded through the mounting holes at the corner of each PCB, as well as the GND terminal on the circuit board, which is connected to the NIM unit's ground terminal. The mounting holes act as a ground via the screws which are used to fix the PCB to the chassis of the NIM unit, thereby grounding the circuit to the unit's chassis.

Currently, only the topmost circuit is in use, as we only ever require one of these circuits to be used at any given time. The choice to use 5 of these circuits was dictated initially by the minimum order quantity, but it makes it far more convenient to switch to a different circuit in the event that the current one breaks. The operation of the circuit fulfills our goals, and we can see the effect of the circuit in (image of pre-stretch and post-stretch signals

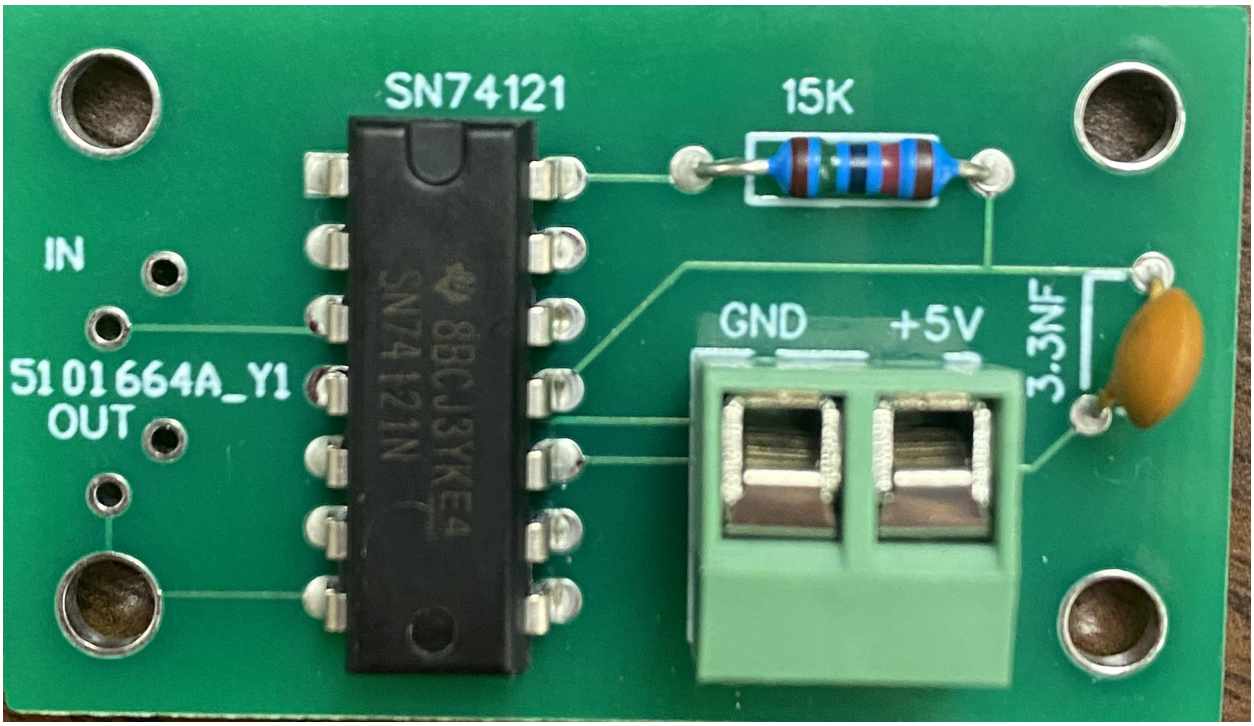

Figure 3.9: Picture of the pulse width extender circuit.

here). This circuit has achieved the desired effect, and has allowed us to conduct coincidence experiments more effectively without introducing any additional noise.

Chapter 4

Characterization of Semiconductor Thin-Film Device Performance

4.1 Semiconductor Background

The primary effort of this thesis was to use our newly-repaired PAS system to characterize the performance of thin-film semiconductor devices, which are of premier importance in the current state of semiconductor technology. These thin-film materials have found a wide range of applications including optical sensors, photovoltaic cells, and batteries, as well as protective and decorative coatings. One of the primary concerns when constructing a semiconductor device is device efficiency. This is especially true of thin-film devices, where optical and photovoltaic applications require that the conversion rate between incident photons and the charge collected at the electrodes be as high as possible. To this end, we focus on two parameters: carrier lifetime and carrier mobility.

Carrier lifetimes are increased mainly by reducing the recombination probability within the material. Recombination in semiconductors happens via a wide range of channels. Here, we concern ourselves only with trap-assisted recombination. Trap-assisted recombination happens when a carrier migrates to a defect site within a semiconductor, and drops into

an inter-band energy level where it becomes stuck and recombines. There is a distinction between deep traps and shallow traps. Shallow traps have an energy difference from the conduction or valence bands which is comparable to the thermal energy, $k_B T$, where deep traps have energy differences far larger than the thermal energy of the material. While carriers can easily escape these shallow traps under the influence of thermal fluctuations, shallow traps have a non-negligible recombination probability, and serve to decrease carrier mobility, thereby decreasing the efficiency of the device. These carrier traps primarily form at two locations within a material: dopant sites and defect sites. Dopant sites are a necessary compromise in extrinsic semiconductor materials. The dopants are required to obtain the desired behavior in the material, and the effect of decreased carrier lifetime because of these dopants cannot be mitigated. Defect sites, however, are unnecessary, and by removing these recombination centers we can improve the carrier lifetimes within the material.

Another important consideration in device efficiency is carrier mobility. When an electron-hole pair (EHP) is generated within a material, these carriers have a limited amount of time before they recombine in a material. This recombination time requires that the carriers within the material move at sufficient speeds such that they don't recombine before they reach the external circuit. Carrier mobility is affected by a wide range of parameters, including the type of material and the defect concentration. Different materials have widely varying carrier mobilities due to different electronic environments. Carrier mobility within these materials can be further increased by reducing defect concentrations. As these carriers travel through the lattice, they scatter from a number of locations including vacancies, impurities, and phonons. Impurities result primarily from dopants which, as previously mentioned, cannot be mitigated, as they're vital to achieving desirable material properties. Phonons, similar to thermal carrier excitations, can be mitigated by cooling the material to low temperature, but are otherwise an intrinsic property of the lattice. Open volume defects, however, can be reduced through a wide range of techniques.

Given that both carrier lifetimes and carrier mobilities depend on defect concentrations, it would seem that PAS, as a non-destructive defect-sensitive technique, would be an optimal candidate for characterizing the quality of semiconductor devices. Additionally, with our depth-resolved capabilities, our apparatus can conduct measurements on specific layers of thin-film devices.

4.2 Energy Calibration

Before any measurements can be made on our sample, we're required to calibrate the energy of our HPGe detector. This calibration process yields two important values: keV per channel and the expected FWHM at 511keV. To accomplish this we use ^{133}Ba and ^{152}Eu as our source of gamma rays of known energies. The reference spectra used to perform our energy calibration are shown in figures 4.1 and 4.2. Here, we can see that the ^{152}Eu spectrum is crowded, making the peaks difficult to identify. For this reason, ^{133}Ba is used to get the keV per channel value, which is then used to identify the peaks in the ^{152}Eu spectrum. Once the peak energies have been found, we can generate a graph of full-width-half-maximum against energy to predict what the expected FWHM at 511keV will be. The expected FWHM tells us what the width of the positron annihilation peak should be were there to be no Doppler broadening. In other words, this tells us the energy resolution of our detector, as the expected FWHM comes only from the detector's energy uncertainty.

To begin the energy calibration procedure, we first collect our ^{133}Ba spectrum, shown in figure 4.3. In this figure, the channel number and FWHM are given by the Maestro software used to collect the spectrum, and the energy of the peaks are determined from the known ^{133}Ba spectrum (note that in both spectra, the 511keV peak is not used in the energy calibration procedure). Using these values of channel number and peak energy, we generate figure 4.5 to find our keV per channel, given by the slopt of the best fit line. In this case, we find that our data acquisition system yields 0.1348keV per channel.

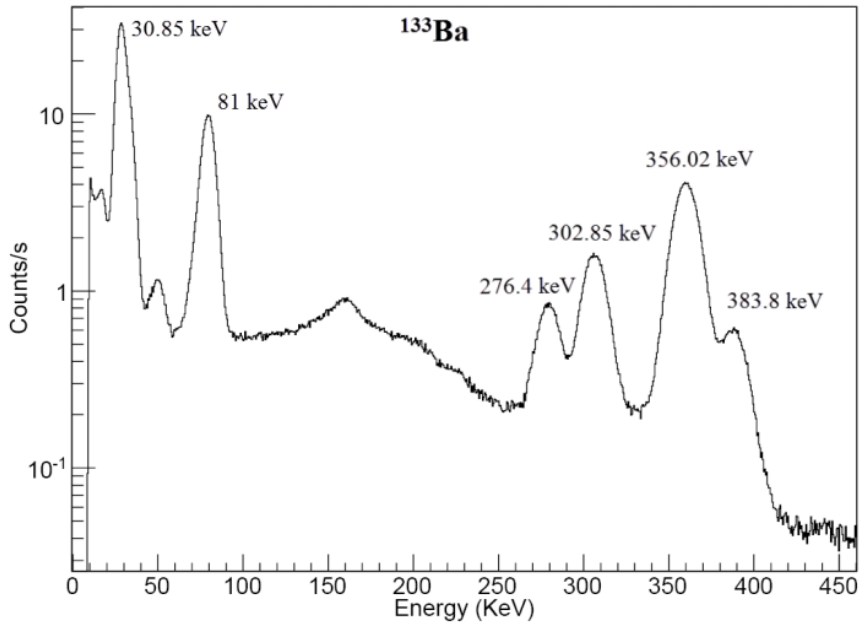

Figure 4.1: ^{133}Ba gamma ray spectrum with labeled peak energies.[37]

Using this conversion rate, we're able to identify the peaks in our ^{152}Eu spectrum, shown in figure 4.4. Again, the channel number and FWHM of these peaks are given by Maestro, and we correlate our calculated peak energies with the reference spectrum in figure 4.2. Then, with the FWHM values from both of our collected spectra, we can plot $\sqrt{E_{peak}}$ vs. FWHM, shown in figure **??**, which gives us an expected FWHM at 511keV of 7.52 channels, or 1.01keV. This expected FWHM defines the energy resolution of our data acquisition system, and is determined by the uncertainty introduced by each of the constiuent components (HPGe detector, spectroscopy amplifier, MCA, etc.).

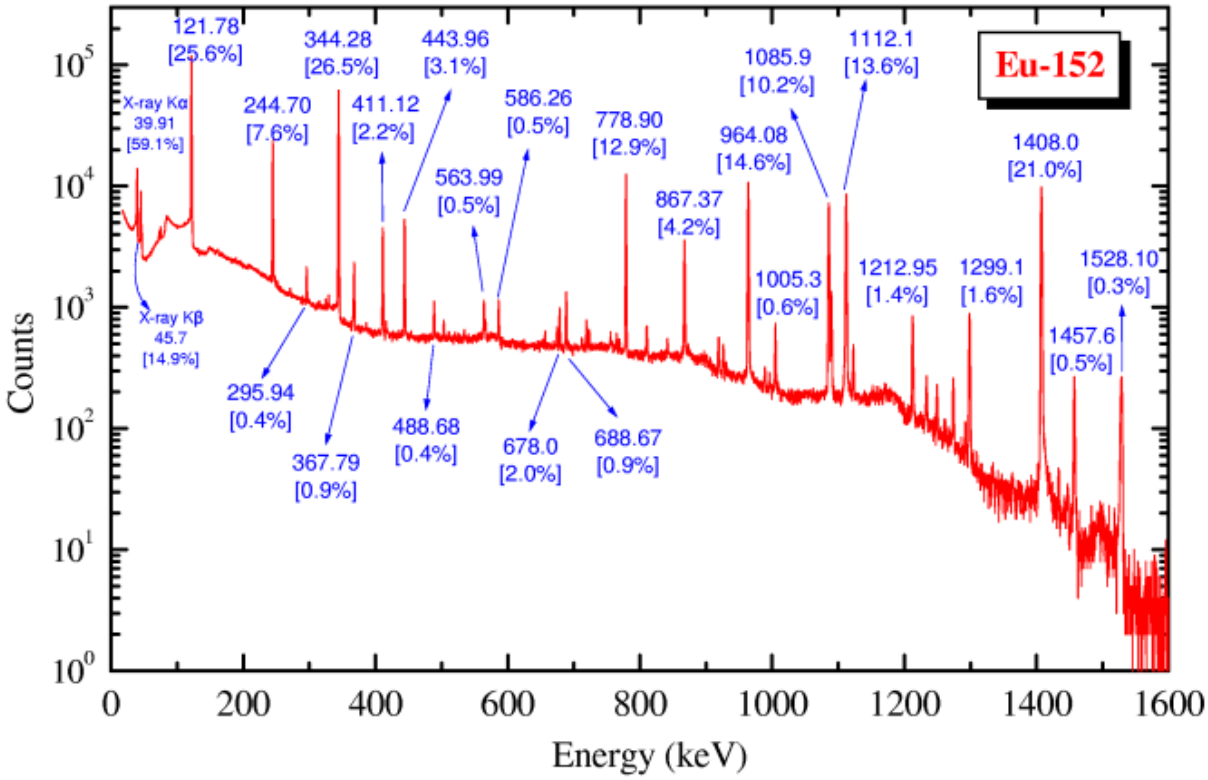

Figure 4.2: ^{152}Eu gamma ray spectrum with labeled peaks energies. [38]

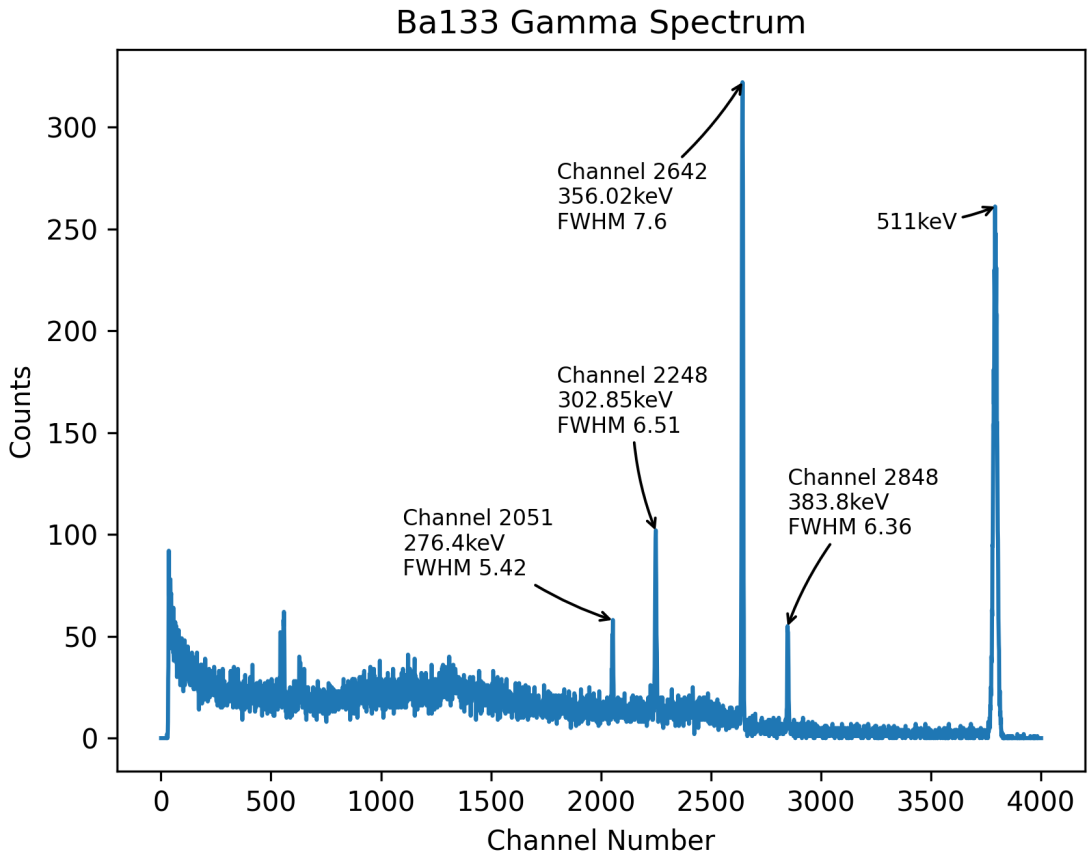

Figure 4.3: ^{133}Ba spectrum collected by our HPGe detector with channel number, peak energy, and FWHM labeled.

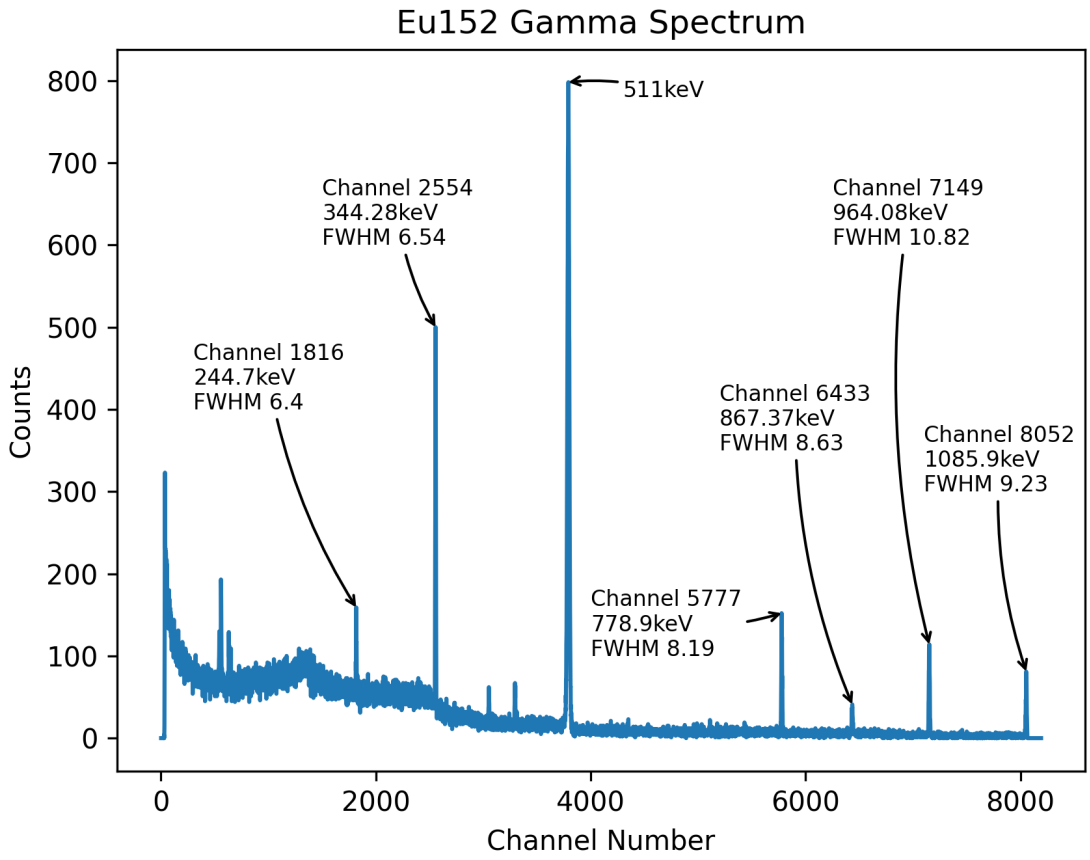

Figure 4.4: ^{152}Eu spectrum collected by our HPGe detector with channel number, peak energy, and FWHM labeled.

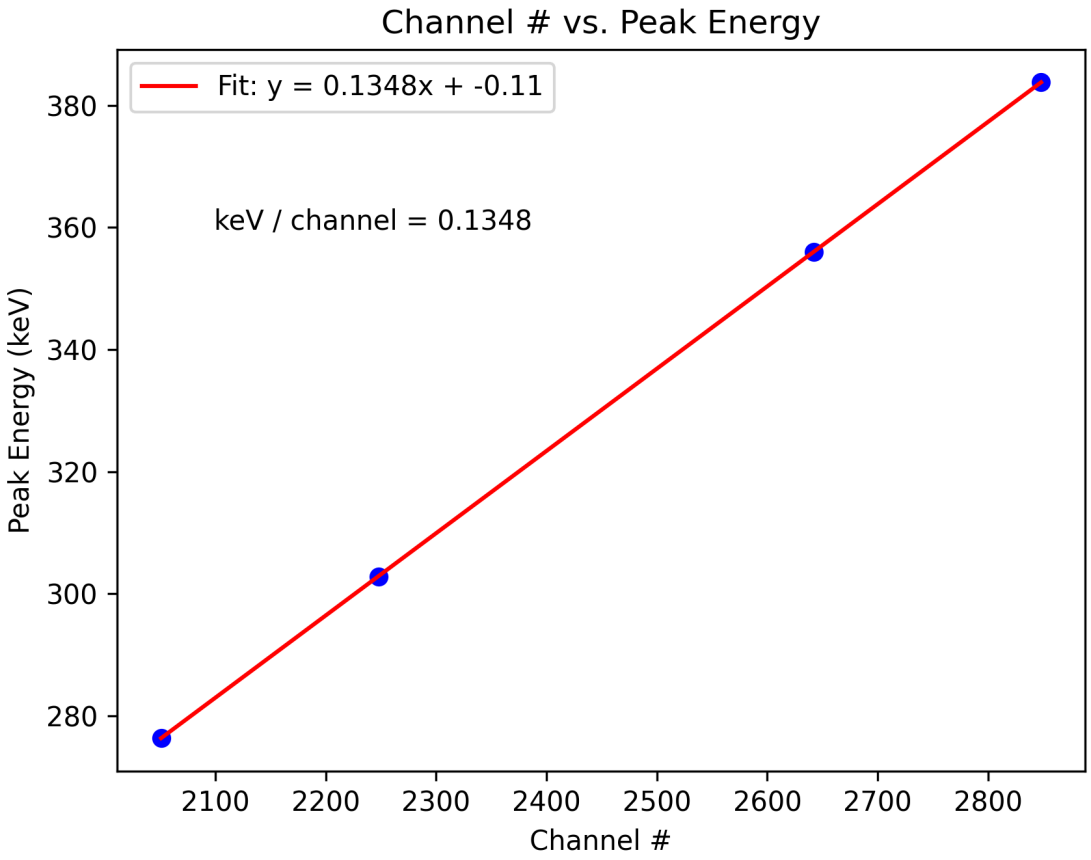

Figure 4.5: Channel number plotted against peak energy. The slope of the best-fit line gives our keV per channel.

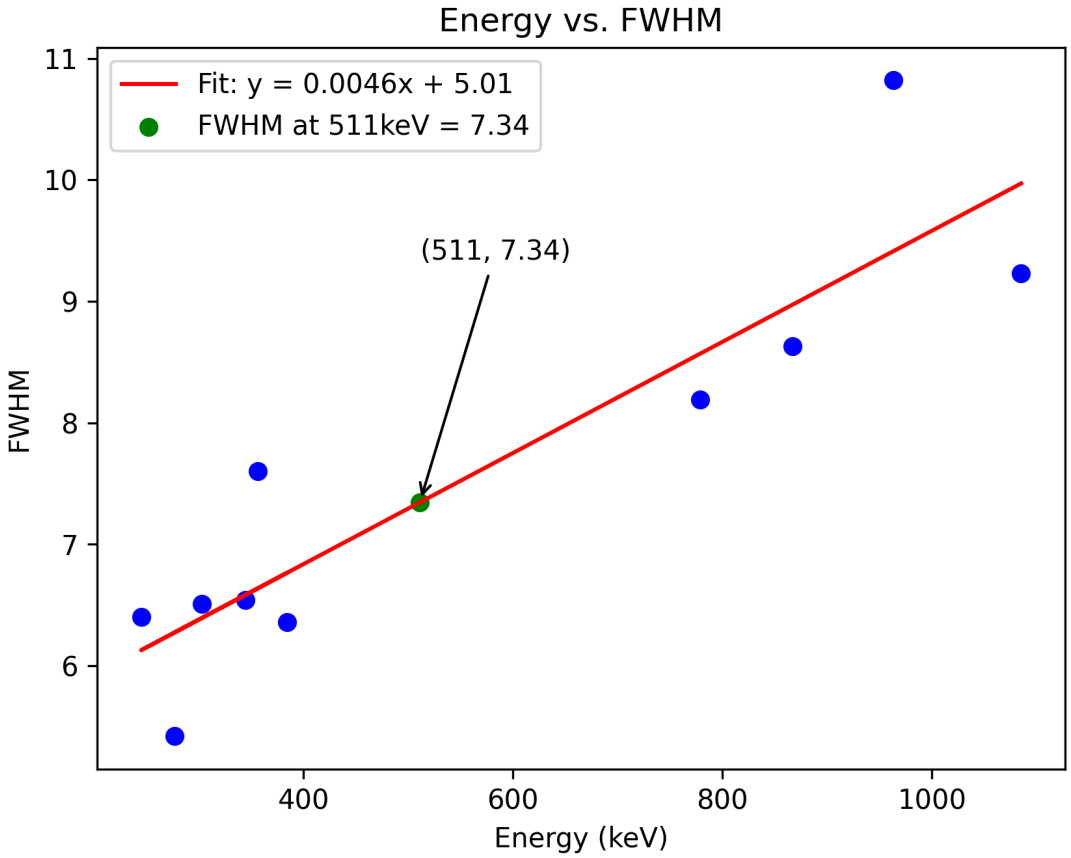

Figure 4.6: E_{peak} plotted against FWHM. The intersection of the best fit line and x = 511 gives our expected FWHM at 511keV with no Doppler broadening.

4.3 Semiconductor Thin Film Analysis

The sample under analysis for this thesis was a multi-layer thin film on a silicon substrate. The material consists of (starting from the topmost layer) 5.5nm ZrO_2, 0.5nm TiN, 5.0nm TiO_2, 300nm SiO_2, followed by a Si substrate. To select for each of these layers, the incident energy of the positrons was adjusted by way of a high-voltage bias applied to the sample biasing rod. Data was collected at 0.25keV, 0.5keV, 0.75keV, 1keV, and 1.5keV. These energies were chosen in order to take measurements within every layer of the material, while minimizing the time required to fully analyze the sample. The penetrating depth of the positrons is estimated using the following equation

$$Z_{mean}(E) = \frac{40E^{1.6}}{\rho} \tag{4.1}$$

where Z_{mean} is the average penetration depth at a given energy in nanometers, E is the positron energy in keV, and ρ is the average density of the material in $g \cdot cm^{-3}$. [13] For this sample, an average density of $5.5g \cdot cm^{-3}$ was used. The depth as a function of energy is shown in figure 4.7, where the red markers indicate energies at which data was collected.

The count rate at the sample during these experiments ranged from 26.5 counts per second (0.25kV) to 29.5 counts per second (1.5kV), and each experiment was run for 2 hours, yielding total count values ranging from 188,605 counts (0.25kV) to 210,133 counts (1.5kV) within the peak region. These spectra can be seen in figure 4.8. The background signal to the left of the 511keV peak is due to positronium formation, insufficient charge collection within the detector, and Compton scattering. The Compton edge can be seen at 340keV.

For each of these energies, we extract the spectrum within the range of 501keV to 521keV by subtracting off the background using an error function, and trimming the data set to within ±10keV of the peak. Using this data set, we're able to calculate the S and W parameters, and generate ratio curves to draw conclusions about the sample under analysis.

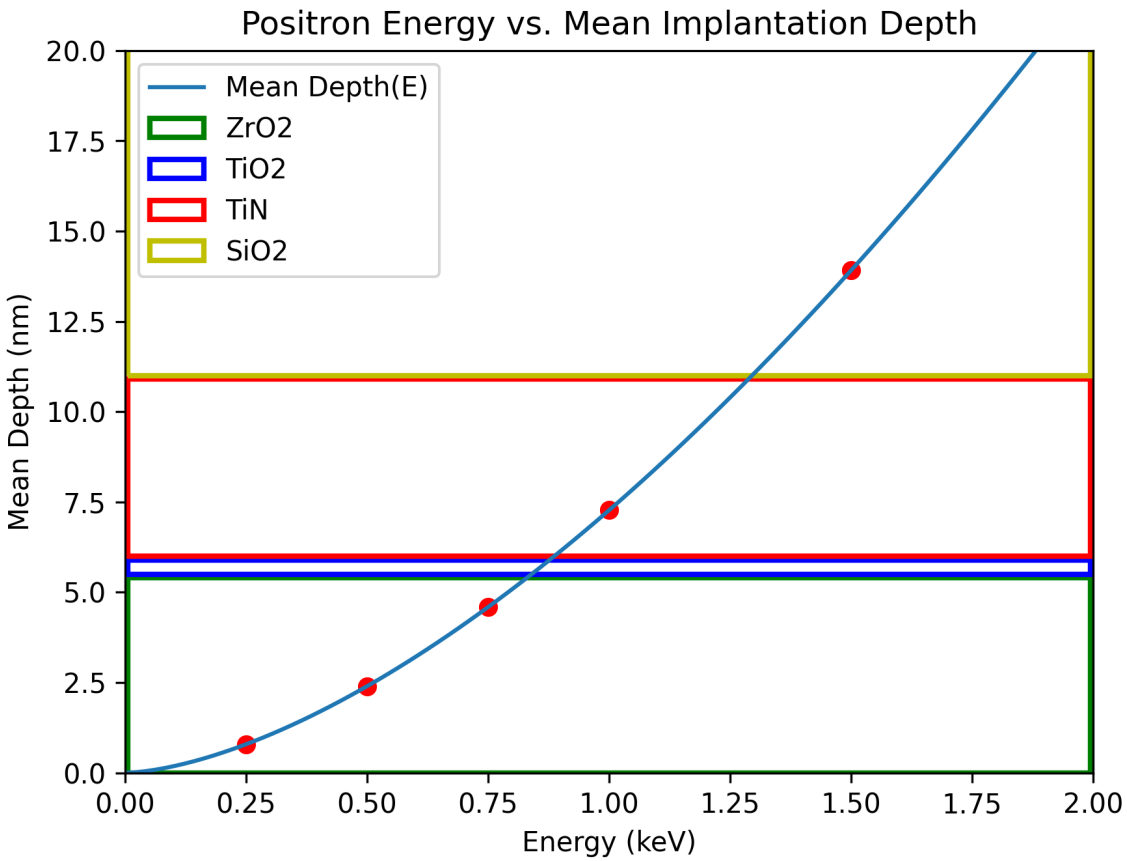

Figure 4.7: Mean penetrating depth of the incident positrons as a function of energy. The red markers indicate energies at which data was collected.

This isolated data set is shown in figure 4.9, which shows all of the 511keV peaks plotted together. Figure 4.10 shows only the right side of these curves, and focuses on the region from the peak to the wing. While we cannot draw any conclusions from either of these figures, these data sets can be used to generate more illustrative charts.

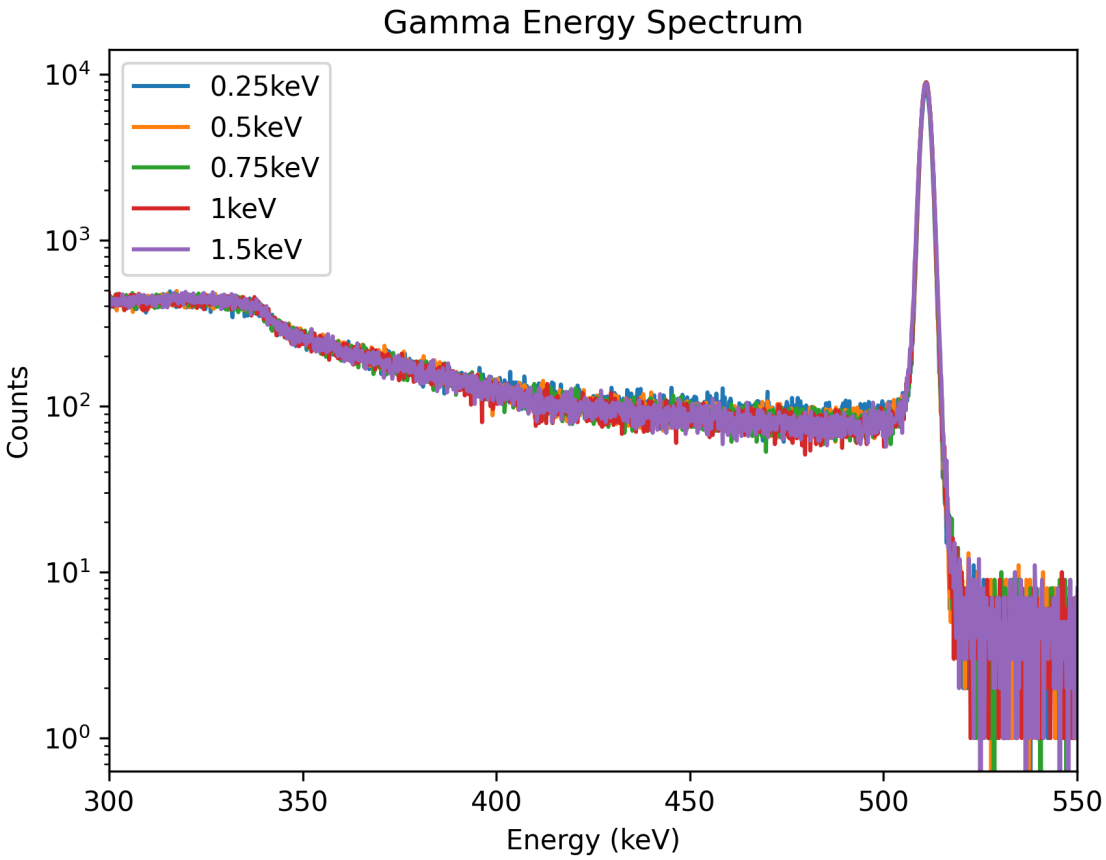

Figure 4.8: Raw gamma ray energy spectrum plotted in log scale.

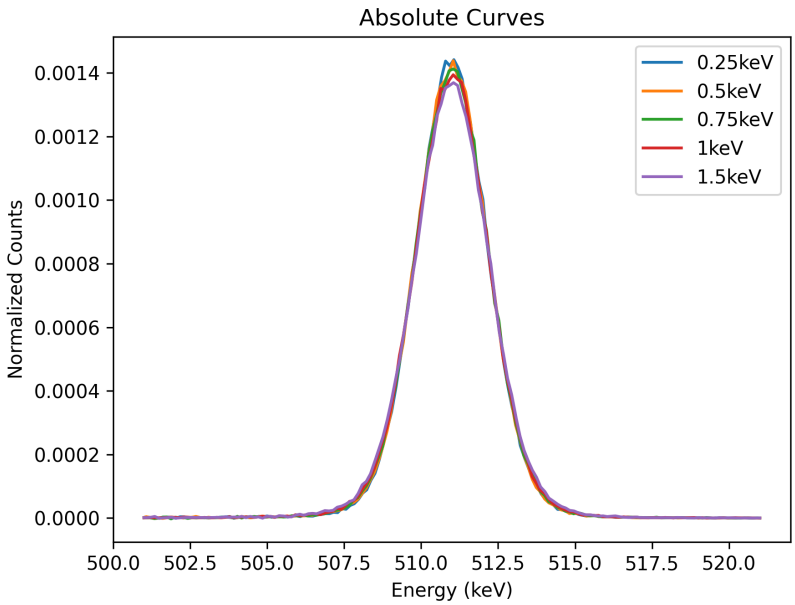

Figure 4.9: 511keV peaks for each energy

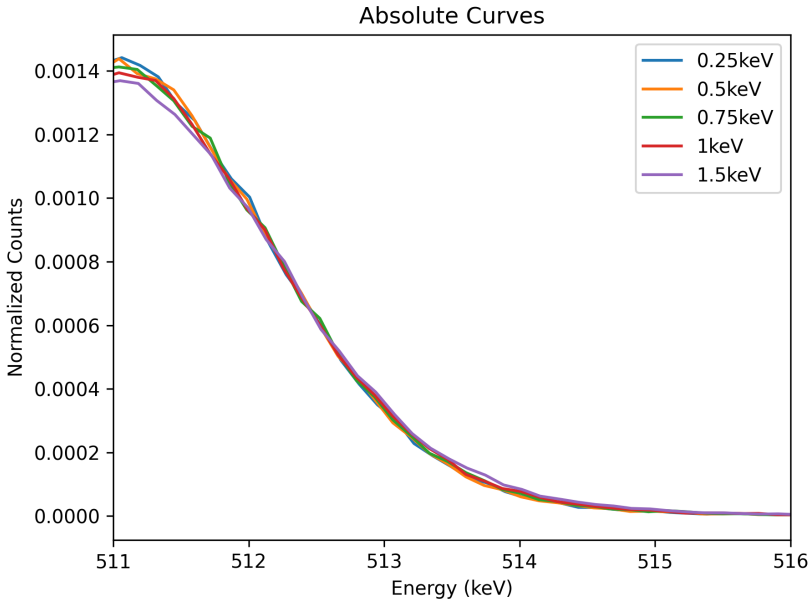

Figure 4.10: Magnified 511keV peaks

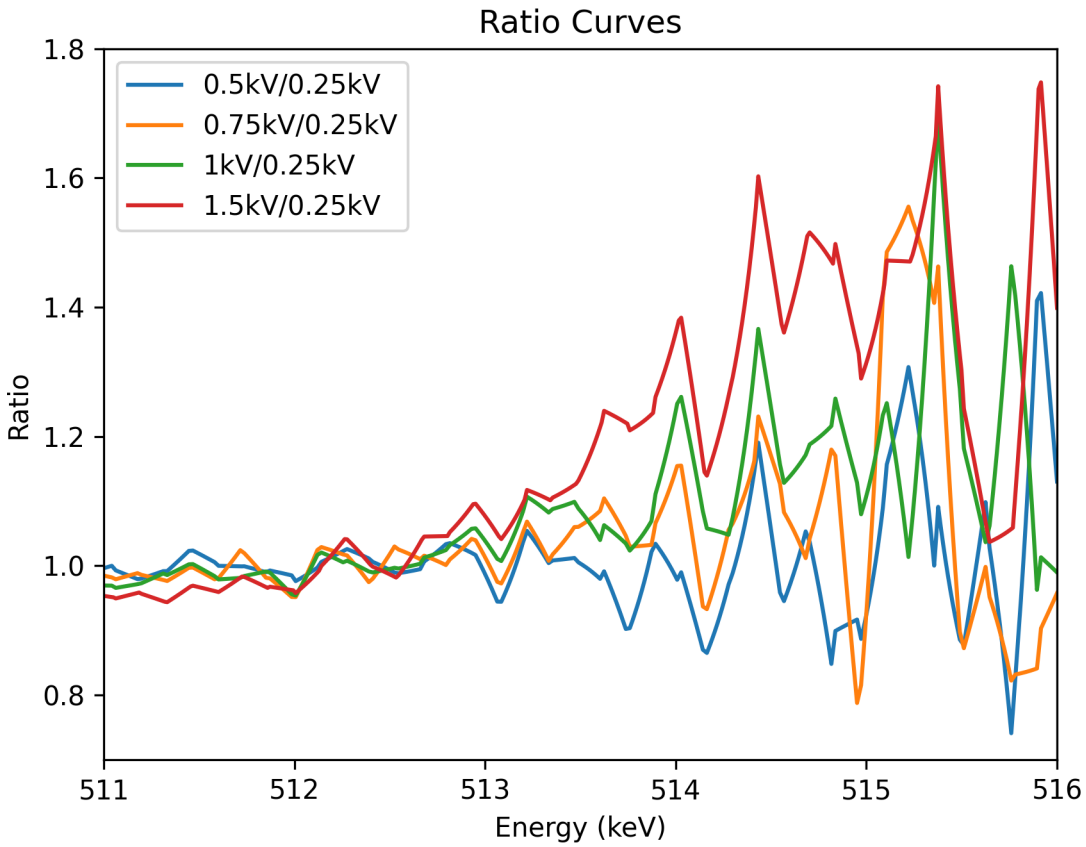

Figure 4.11: Ratio curves for the ZrO_2 thin film material

By taking the ratio of each of these data sets to the values of the lowest energy curve (0.25kV), we can more clearly illustrate the differences between each of these curves. These ratio curves are shown in figure 4.11. From this, we can more clearly see the differences in the spectra for each energy. The change in these spectra as a function of energy is caused by a change in the chemical environment in which the positron annihilates. These ratio curves clearly demonstrate that we're penetrating deeper into the material, and that we're observing a different chemical environment at each of these depths, as we would expect given the structure of the sample under analysis.

Further, we can combine these ratio curves with calculations of the S and W parameters, which are shown in figures 4.12 and 4.13, respectively. Here, the S parameter region is defined as being within ±1keV of the peak, and the total peak region is defined as being

within ±10keV of the center of the peak. As discussed in the opening chapter of this thesis, a higher S parameter (and lower W parameter) corresponds to annihilation with valence-band electrons, implying the presence of open-volume defects. As the surface is an open-volume defect with infinite radius, the contribution to the S parameter from the surface states results in a high S parameter at low energies. The S parameter can be seen to decrease rapidly (and the W parameter seen to increase) as the penetration depth of the positrons increases.

The error bars for the S and W parameter are a standard error calculation, given by equations 4.2 and 4.3

$$\Delta S = S \cdot \sqrt{\frac{1}{N_s} + \frac{1}{N}} \tag{4.2}$$

$$\Delta W = W \cdot \sqrt{\frac{1}{N_w} + \frac{1}{N}} \tag{4.3}$$

Where S and W are the values of the S and W parameter for a given measurement, N_s and N_w are the number of counts in the S and W regions, and N is the total number of counts under the peak.

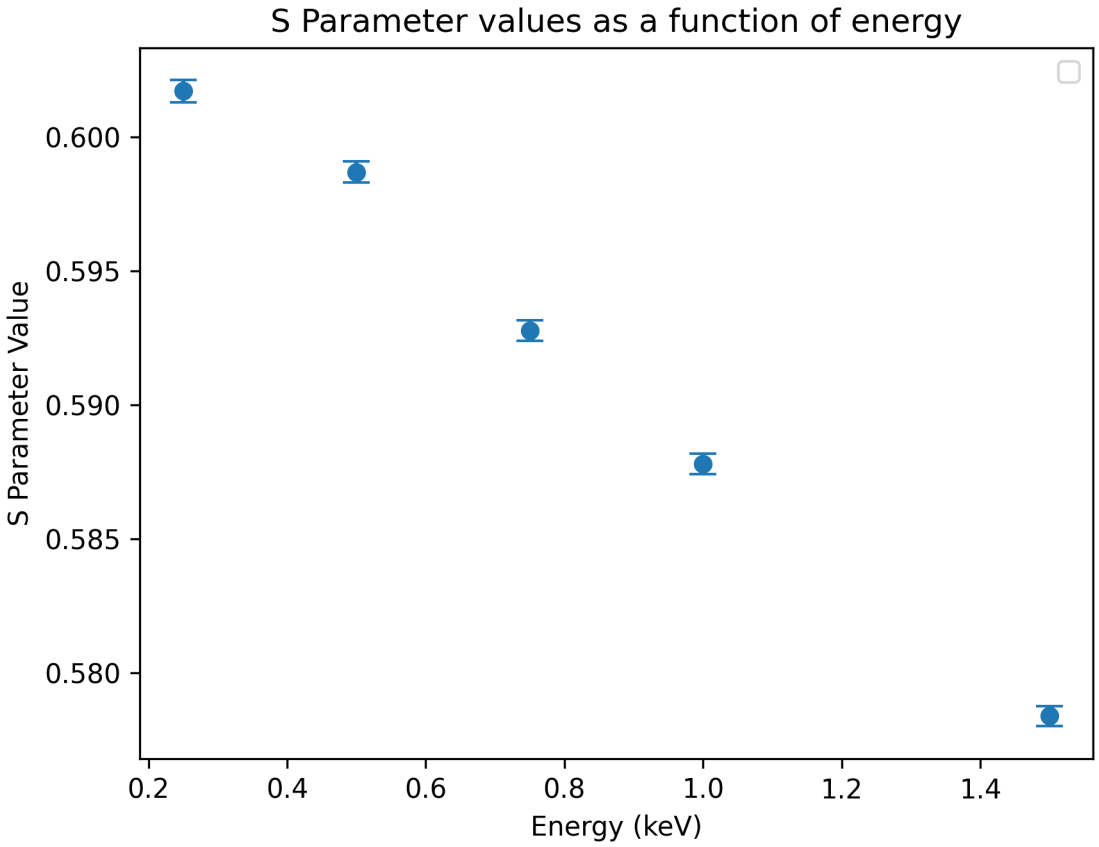

Figure 4.12: Calculated S parameter as a function of incident positron energy.

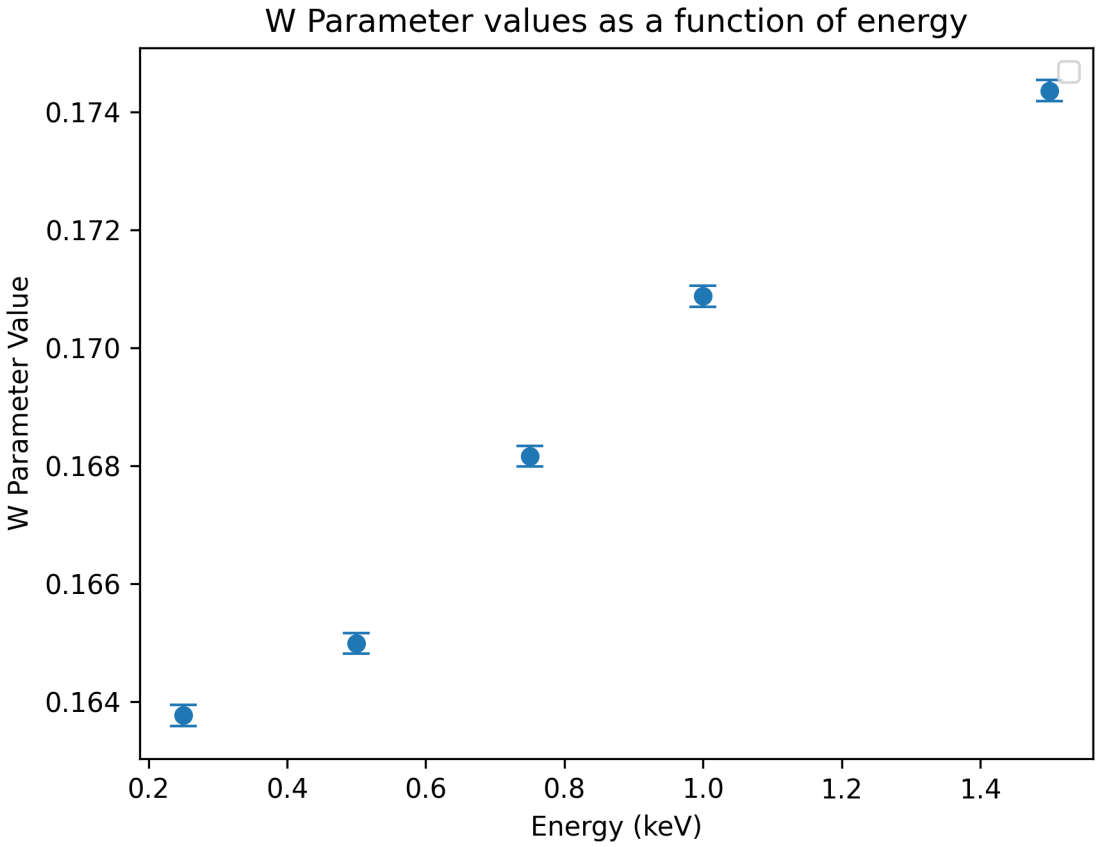

Figure 4.13: Calculated W parameter as a function of incident positron energy.

Chapter 5

Conclusions and Further Work

This thesis presents the repair and recommissioning of the variable-energy positron beamline, as well as a new application of the beam in the study of semiconductor thin films.

The repair of the RGM system allowed for the return-to-service of the positron beam in order to conduct these measurements. The RGM system was thoroughly tested to ensure it was stable and in working order.

Additionally, the pulse-width-stretcher which was designed and assembled to extend the timing signal produced by the NaI detector will allow for future gamma ray coincidence measurements to be performed.

The results presented in this thesis demonstrate the ability for PAS techniques to be applied to the study and improvement of semiconductor thin-film devices. As a non-destructive depth-resolved defect characterization technique, PAS can isolate specific layers within a multi-layer material with accuracy on the order of a few nanometers. This ability was demonstrated by presentation of the ratio curves, which shows a continual change in the chemical composition as a function of sample bias (and therefore incident positron energy), confirming our hypothesis that PAS can be used to probe specific layers of the material. Furthermore, the S and W parameter calculations can allow us to draw conclusions about the defect characteristics within specific layers of the material.

This is an exciting application of this technique, as it allows for a new avenue for the optimization of the semiconductor manufacturing process with regards to multi-layer thin-films. By exploring a wide range of manufacturing parameters (deposition type, time, temperature, annealing temperature, etc.), PAS can be used to optimize the process by identifying the defect concentrations which result from a change in each of these parameters. Furthermore, it can do this on a layer-by-layer basis, allowing the parameters to be optimized for the entire as-grown thin-film stack.

Experiments planned for the future include exploring the possibility for PAS to characterize the effect of post-manufacturing defect passivation, specifically with regards to hydrogen passivation. Hydrogen passivation is a technique whereby hydrogen ions are implanted into open-volume defects in order to "smooth out" the negative potential wells formed by these defects. The group postulates that this hydrogen passivation technique will be visible in the Doppler-broadening spectrum, opening yet more possible avenues of investigation for widening the applications of this technique.

Bibliography

[1] Paul Adrien Maurice Dirac. The quantum theory of the electron. *Proceedings of the Royal Society of London. Series A, Containing Papers of a Mathematical and Physical Character*, 117(778):610–624, 1928.

[2] Carl D Anderson. The positive electron. *Physical Review*, 43(6):491, 1933.

[3] Shunji Adachi, Masami Chiba, Tachishige Hirose, Shojiro Nagayama, Yuki Nakamitsu, Toshiyuki Sato, and Tadashi Yamada. Measurement of e+ e- annihilation at rest into four γ rays. *Physical review letters*, 65(21):2634, 1990.

[4] JK Basson. Direct quantitative observation of the three-photon annihilation of a positron-negatron pair. *Physical Review*, 96(3):691, 1954.

[5] T Mankamo and P Jauho. Measurements of the momentum correlation in the three-photon annihilation of positronium. *Nuclear Physics A*, 158(2):487–496, 1970.

[6] Manori Prasadika Nadesalingam. *Study of positron trapping at quantum-dot like copper particles on the surface of iron using positron annihilation induced auger electron spectroscopy*. PhD thesis, The University of Texas at Arlington, 2003.

[7] S DeBenedetti, CE Cowan, and WR Konneker. Angular distribution of annihilation radiation. *Physical Review*, 76(3):440, 1949.

[8] Savely G Karshenboim. Precision study of positronium: Testing bound state qed theory. *International Journal of Modern Physics A*, 19(23):3879–3896, 2004.

[9] Filip Tuomisto and Ilja Makkonen. Defect identification in semiconductors with positron annihilation: Experiment and theory. *Reviews of Modern Physics*, 85(4):1583, 2013.

[10] FA Selim. Positron annihilation spectroscopy of defects in nuclear and irradiated materials-a review. *Materials Characterization*, 174:110952, 2021.

[11] P Horodek, M Bugdol, AG Kobets, IN Meshkov, OS Orlov, A Yu Rudakov, AA Sidorin, and SL Yakovenko. Development of positron annihilation spectroscopy at lepta facility. *Physics of Particles and Nuclei Letters*, 11:708–712, 2014.

[12] Dipankar Chattarji. *The theory of Auger transitions*. Elsevier, 2012.

[13] Peter J Schultz and Kelvin G Lynn. Interaction of positron beams with surfaces, thin films, and interfaces. *Reviews of Modern Physics*, 60(3):701, 1988.

[14] Kjeld O Jensen and AB Walker. Positron thermalization and non-thermal trapping in metals. *Journal of Physics: Condensed Matter*, 2(49):9757, 1990.

[15] RM Nieminen and J Oliva. Theory of positronium formation and positron emission at metal surfaces. *Physical Review B*, 22(5):2226, 1980.

[16] Martti J Puska and Risto M Nieminen. Theory of positrons in solids and on solid surfaces. *Reviews of modern Physics*, 66(3):841, 1994.

[17] Werner Brandt and Néstor R Arista. Diffusion heating and cooling of positrons in constrained media. *Physical Review A*, 19(6):2317, 1979.

[18] MJ Puska and RM Nieminen. Defect spectroscopy with positrons: a general calculational method. *Journal of Physics F: Metal Physics*, 13(2):333, 1983.

[19] Roberto Sennen Brusa, W Deng, GP Karwasz, and Antonio Zecca. Doppler-broadening measurements of positron annihilation with high-momentum electrons in pure elements. *Nuclear Instruments and Methods in Physics Research Section B: Beam Interactions with Materials and Atoms*, 194(4):519–531, 2002.

[20] PA Sterne, P Asoka-Kumar, and RH Howell. Atomic-based calculations of two-detector doppler-broadening spectra. *Applied surface science*, 194(1-4):71–75, 2002.

[21] Keun-ho Lee. *The relative intensity of positron annihilation-induced auger electron emission from iron, copper, palladium and gold*. PhD thesis, The University of Texas at Arlington, 1990.

[22] Christoph Hugenschmidt. Positrons in surface physics. *Surface Science Reports*, 71(4):547–594, 2016.

[23] Randall Wayne Gladen. *Development and Applications of a Multi-Functional Positron Beam for Spectroscopies of Surfaces and Interfaces*. The University of Texas at Arlington, 2019.

[24] Nucleonica. `https://nucleonica.com/`. Accessed: 11-17-2023.

[25] Shuping Xie. *Positron annihilation induced Auger electron spectroscopy of inner shell transitions using the time-of-flight technique*. The University of Texas at Arlington, 2002.

[26] Manori Prasadika Nadesalingam. *Study of oxide surfaces using time of flight positron annihilation induced Auger electron spectroscopy*. The University of Texas at Arlington, 2007.

[27] YC Wu, YQ Chen, SL Wu, ZQ Chen, SJ Wang, and RG Greaves. High moderation efficiency positron beamline. *physica status solidi c*, 4(10):4032–4035, 2007.

[28] Advanced Research Systems. *ARS Operation Manual Expanders Models DE-202 and DE-204*.

[29] John David Jackson. Classical electrodynamics, 1999.

[30] Michael A Lieberman and Allan J Lichtenberg. Principles of plasma discharges and materials processing. *MRS Bulletin*, 30(12):899–901, 1994.

[31] Ekram Husain and RS Nema. Analysis of paschen curves for air, n2 and sf6 using the townsend breakdown equation. *IEEE transactions on electrical insulation*, (4):350–353, 1982.

[32] RG Greaves and CM Surko. Solid neon moderator for positron-trapping experiments. *Canadian Journal of Physics*, 74(7-8):445–448, 1996.

[33] M Moszyniski, A Nassalski, A Syntfeld-Kazuch, L Swiderski, and T Szczecsniak. Energy resolution of scintillation detectors—new observations. *IEEE Transactions on Nuclear Science*, 55(3):1062–1068, 2008.

[34] Stephen E Derenzo, Woon-Seng Choong, and William W Moses. Fundamental limits of scintillation detector timing precision. *Physics in Medicine & Biology*, 59(13):3261, 2014.

[35] Ortec. `https://ortec-online.com/`. Accessed: 11-18-2023.

[36] Glenn F Knoll. *Radiation detection and measurement*. John Wiley & Sons, 2010.

[37] Zhang Dali, Shao-Lin Xiong, Fan-Zhang, Yanguo-Li, Zheng-Hua An, Yan-Bing Xu, and Xilei Sun. Energy response of gecam x and gamma-ray detector prototype. 04 2018.

[38] Ammar Battawy. *Internal and External Radiation Exposure Evaluation Amongst Selected Workers and Locations in Iraq*. PhD thesis, 08 2013.